Department of Physics and Astronomy
Heidelberg University

Master thesis

in Physics

submitted by

Christian-Marcel Schmied

born in Gummersbach (Germany)

2016

Emergence of Structure in a Quenched (Quasi) One-dimensional Spin-1 Bose-Einstein Condensate in Comparison with Experiments

This Master thesis has been carried out by Christian-Marcel Schmied

at the

Kirchhoff-Institute of Physics, Heidelberg University

under the supervision of

Prof. Dr. Thomas Gasenzer

Abstract

In this thesis, we numerically study the emergence of structure in a (quasi) one-dimensional spin-1 Bose-Einstein condensate after a sudden change of a Hamiltonian parameter, which we call quench. We apply the Truncated Wigner Approximation to simulate the equations of motion in presence of a trapping potential. We want to enable direct quantitative comparison to experiments, peformed with ^{87}Rb atoms confined in a longitudinal cigar-shaped trap. We show, that it is essential to use a quasi one-dimensional description of the dynamics by means of the non-polynomial Schrödinger equation which includes excitations in the transversal direction of the trap. Setting the initial quantum noise into single-particle eigenmodes of the effective potential leads to good agreement of the dynamical timescales between simulations and experiments. In the limit of a small depletion of the condensate, the dynamics is theoretically described by Bogoliubov theory. Due to the sudden quench, unstable momentum modes are predicted. These are populated by spin-changing collisions. The resulting characteristic structure size of the system, associated with its spin domain size, can be observed in the transversal spin direction with the help of the auto-correlation function. For short times, it fits well to the Bogoliubov prediction. For later times we see deviations, which we attribute to an effective change of the spin interaction strength.

Zusammenfassung

In dieser Arbeit untersuchen wir die Strukturentstehung in einem (quasi) eindimensionalen Spin-1 Bose-Einstein Kondensat nach einer schnellen Änderung eines Parameters im Hamiltonian, Quench genannt. Wir verwenden die Truncated Wigner Näherung, um die Bewegungsgleichungen im Fallenpotential zu simulieren. Wir wollen einen direkten quantitativen Vergleich mit Experimenten ermöglichen, die mit ^{87}Rb Atomen, die in einer longitudinalen, Zigarren-förmigen Falle gehalten werden, durchgeführt werden. Wir zeigen, dass es notwendig ist eine quasi eindimensionale Beschreibung der Dynamik mittels der Nicht-polynomialen Schrödinger Gleichung, die Anregungen in der transversalen Fallenrichtung berücksichtigt, zu verwenden. Setzen des Anfangsquantenrauschens in die Einteilchen-Eigenmoden des effektiven Potentials führt zu guter Übereinstimmung der dynamischen Zeitskalen zwischen Simulation und Experiment. Im Limit geringer Leerung des Kondensats, wird die Dynamik theoretisch durch Bogoliubov Theorie beschrieben. Aufgrund der schnellen Parameterveränderung sind instabile Impulsmoden vorhergesagt. Diese werden mit spinverändernden Kollisionen besetzt. Die resultierende charakteristische Strukturgröße des Systems, die mit seiner Spindomänengröße assoziiert wird, kann in transversaler Spinrichtung mit Hilfe der Auto-Korrelationsfunktion beobachtet werden. Für kurze Zeiten passt diese gut zur Bogoliubov Vorhersage. Für spätere Zeiten sehen wir Abweichungen, die wir einer effektiven Änderung der Spinwechselwirkungsstärke zuschreiben.

Contents

1 Introduction

Because of the high degree of experimental control over the relevant system parameters, ultracold quantum gases can be used as model systems for studying non-equilibrium dynamics.
Especially Bose gases with spin degrees of freedom, which are called spinor Bose gases, offer the great possibility to investigate different non-equilibrium phenomena as they exhibit a wealth of phase transitions, that have been studied in [1, 2, 3].
After preparing the system in the many-body ground state of a certain Hamiltonian parameter set, it can be driven out of equilibrium by changing one or several parameters such that we end up in another phase with a different ground state. If a parameter is changed instantaneously, we call it a sudden quench. Analysing the properties of spinor Bose gases after performing a quench, the formation of topological defects [4] as well as universal scaling in the dynamics [5] have been observed.
In spin-1 Bose gases, whose components are given by the three magnetic sublevels of the $F = 1$ hyperfine manifold, two different meanfield ground states can be found in case of antiferromagnetic interactions [6]. Depending on the quadratic Zeeman energy q, which is proportional to the external magnetic field, the system is either in the polar or the paramagnetic phase. By quenching from the polar into the paramagnetic phase, instabilities are introduced by spin-changing collisions [2]. Exponential growth of the corresponding unstable momentum modes leads to structure formation in the transversal spin direction [1]. Analytical predictions for the unstable momentum modes on short timescales are given by Bogoliubov theory [6, 7] only in case of zero trapping potential, i. e. for a homogeneous system. As Bogoliubov theory considers small fluctuations around a meanfield state, we expect it to break down at times where the fluctuations in the system become macroscopically large.
To make analytical predictions for such a complicated many-body system is impossible in presence of a trapping potential. Therefore numerical methods are needed to enable quantitative comparisons to experiments performed with spin-1 Bose gases as the atoms are confined in traps. If the important part of the dynamics takes place in the region of

highly occupied modes, it has been shown that the time evolution is well described by classical fields [8, 9, 10]. In this case the semi-classical Truncated Wigner method [10, 11, 12, 13] can be used to numerically study dynamical features of the system. The method is based on evolving samples of classical fields, whose initial configuration is composed of a meanfield state and quantum fluctuations, in time. Physical quantities are then obtained by averaging these samples. Comparing numerical simulations in presence of a trapping potential to simulations in a homogeneous setup, enables to directly identify trap effects. To make reliable predictions for times beyond the Bogoliubov regime, it is essential to investigate if the characteristic dynamics on short timescales, which have also been observed in experiments [14], can be captured with such numerical simulations.

In this work, we numerically study the emergence of structure at short times after a sudden quench of the magnetic field in an antiferromagnetic spin-1 Bose gas in one spatial dimension. As we expect the important part of the dynamics to take place in the region of highly occupied modes, we apply the Truncated Wigner method to simulate the equations of motion in presence of a trapping potential. We compare our results to experiments performed by the group of Prof. Dr. Markus K. Oberthaler. In the experimental setup, ^{87}Rb atoms are confined in a longitudinal cigar-shaped trap. Recent experimental results, including the data we used for comparison, can be found in [14].

In chapter 2, we discuss the underlying theoretical concepts. As we aim to quantify whether excitations in the transversal direction of the trap play a role in the experiment, we consider two different descriptions of the system. Assuming a strictly one-dimensional setting, where the system is transversally in the ground state, the time evolution is given by the Gross-Pitaevskii equation (GPE). If we allow for excitations in the transversal direction of the trap, we obtain that the system, which we call quasi one-dimensional, is described by the non-polynomial Schrödinger equation (NPSE). Then we explain the meanfield phase diagram and illustrate the notion of a sudden quench of the magnetic field from the polar into the paramagnetic phase. Applying homogeneous Bogoliubov theory leads to analytical predictions for the dynamics on short timescales.

In chapter 3, we describe the simulation methods. As we expect the important part of the dynamics to take place in the region of highly occupied modes, we use the semi-classical Truncated Wigner Approximation (TWA). The method leads to approximative equations of motion for the Wigner function, which is the phase space representation of the density matrix. Instead of evolving the Wigner function in time, we propagate samples of classical fields whose initial probability distributions are given by the Wigner

function. We find that the equations of motion for the fields within the TWA are the Gross-Pitaevskii equations for one-dimensional and the non-polynomial Schrödinger equations for quasi one-dimensional settings. The initial configuration of the fields is composed of the initial meanfield state of the system and quantum fluctuations which are sampled from the Wigner function of the vacuum. Thus the TWA allows for predictions beyond the meanfield approximation. We present two different approaches for the sampling of the quantum noise. To perform the time integration of the equations of motion, we discuss the Fourier split-step method. We determine the initial meanfield state, which is the ground state in the polar phase, by means of imaginary time propagation (ITP).

In chapter 4 we show results of comparing the emergence of structure at short times after the sudden quench between simulation and experiment. To enable a quantitative comparison, we first investigate whether transversal excitations are present in the experimental setup. We find that the quasi one-dimensional description by means of the non-polynomial Schrödinger equation (NPSE) is the appropriate model to recover the experimental dynamics. We pursue with introducing the transversal spin as a suited observable for analysing the dynamics on short timescales as Bogoliubov excitations occur in the transversal spin direction. We then present how to mimic the experimental measurement of the transversal spin. For direct quantitative comparisons of simulations to the experiment, we analyse the auto-correlation function and the corresponding Fourier spectra of the transversal spin for short evolution times. We present results of simulations performed with two different samplings of the initial quantum noise. We find that sampling the noise into the single particle eigenmodes of the effective potential for the $m_F = \pm 1$ components leads to good agreement between simulation and experiment for some of the selected evolution times. Using the Fourier mode sampling, the structure formation in the simulation is way faster than in the experiment. In addition, we compare numerical simulations to the homogeneous Bogoliubov theory. For short times we find that the data follows the Bogoliubov prediction in the quench parameter regime $-q > nc_1$. At later times we expect deviations. However, we find that the structure size is again well described by Bogoliubov theory with a smaller spin interaction strength nc_1.

We conclude with an outlook on future projects concerning the properties of spinor Bose gases at evolution times beyond the Bogoliubov regime.

2 Theoretical concepts

As we aim to study non-equilibrium dynamics of trapped spin-1 Bose-Einstein condensates (BEC) in (quasi) one-dimensional settings, we investigate the underlying theoretical concepts in this chapter. We start with the three-dimensional action functional of a spin-1 Bose gas in order to derive the corresponding (quasi) one-dimensional description. Assuming a strictly one-dimensional setting, where the system is transversally in the ground state, the time evolution is given by the Gross-Pitaevskii equation (GPE). If we allow for excitations in the transversal direction of the trap, we obtain that the system, which we call quasi one-dimensional, is described by the non-polynomial Schrödinger equation (NPSE). Performing simulations with both sets of equations of motion enables to identify if transversal excitations play a role in experiments performed by the group of Prof. Dr. Markus K. Oberthaler, where they study quench dynamics in ^{87}Rb in the hyperfine manifold $F = 2$. Since the $m_F = \pm 2$ states are energetically tuned far away by means of magnetic fields, they are not populated during the time evolution resulting in a system being described by an effective spin-1 Hamiltonian. Thus we adapt our bare spin-1 model to an effective description. With this at hand, we explain the accessible meanfield phase diagram of the system. Thereto we discuss the initially prepared state and the concept of a sudden parameter quench. We close the chapter by applying Bogoliubov theory to figure out the instabilities of the system emerging on short timescales after the quench. These instabilities play an important role for the structure formation.

2.1 (Quasi) one-dimensional equations of motion of a spin-1 BEC

For deriving the (quasi) one-dimensional equations of motion of a spin-1 BEC, we mainly follow the approach presented in [15] and [16]. Assuming a strictly one-dimensional setting, where the system is transversally in the ground state, the time evolution is given by the Gross-Pitaevskii equation (GPE). If we allow for excitations in the transversal direction of the trap, we obtain that the system, which we call quasi one-dimensional,

is described by the non-polynomial Schrödinger equation (NPSE). In chapter 4, we present results of simulations performed with both sets of equations of motion with which we are able to identify if transversal excitations play a role in the above mentioned experiment. We find that transversal excitations are indeed relevant in the experiment, as the experimentally observed dynamics fits well to the results of NPSE simulations.

2.1.1 3D action functional

The three-dimensional action functional of a spin-1 BEC reads (summation over repeated indices implied)

$$S = \int \mathrm{d}t\, \mathrm{d}\vec{r} \left[\hat{\Psi}_m^\dagger \left(i\hbar \frac{\partial}{\partial t} + \frac{\hbar^2}{2M}\nabla^2 - V_{\mathrm{ext}} \right) \hat{\Psi}_m - \hat{\Psi}_m^\dagger q \left(f_z^2\right)_{ml} \hat{\Psi}_l \right.$$
$$\left. - \frac{c_0}{2} \hat{\Psi}_m^\dagger \hat{\Psi}_l^\dagger \hat{\Psi}_l \hat{\Psi}_m - \frac{c_1}{2} \hat{\Psi}_l^\dagger \hat{\Psi}_j^\dagger \left(f_\alpha\right)_{jk} \left(f_\alpha\right)_{lm} \hat{\Psi}_k \hat{\Psi}_m \right], \tag{2.1}$$

where $\hat{\Psi}_m(\vec{r},t)$ and $\hat{\Psi}_m^\dagger(\vec{r},t)$ are the bosonic field operators that annihilate and, respectively, create an atom in the mth internal state at spatial location $\vec{r}$ and time t. $m = \pm 1, 0$ labels the three magnetic sublevels of the $F = 1$ hyperfine manifold. M is the mass of an atom and $V_{\mathrm{ext}}(\vec{r})$ denotes the external trapping potential. The quadratic Zeeman energy q, which is proportional to the magnetic field, can be calculated using the Breit-Rabi formula [17]. A sudden change of the magnetic field, which we call quench, enables to study the non-equilibrium dynamics of the system. The linear Zeeman shift is absorbed by transforming into the rotating frame of reference.
The interaction strengths c_0 for the density-density coupling and c_1 for the spin-spin coupling are given by

$$c_0 = \frac{g_0 + 2g_2}{3}, \qquad c_1 = \frac{g_2 - g_0}{3}, \tag{2.2}$$

where $g_i = \frac{4\pi\hbar^2 a_i}{M}$ with a_i the s-wave scattering length of the symmetric spin channel with total spin i [18].
$f_{\alpha=x,y,z}$ are the spin-1 matrices, which can be written as

$$f_x = \frac{1}{\sqrt{2}} \begin{pmatrix} 0 & 1 & 0 \\ 1 & 0 & 1 \\ 0 & 1 & 0 \end{pmatrix}, \quad f_y = \frac{i}{\sqrt{2}} \begin{pmatrix} 0 & -1 & 0 \\ 1 & 0 & -1 \\ 0 & 1 & 0 \end{pmatrix}, \quad f_z = \begin{pmatrix} 1 & 0 & 0 \\ 0 & 0 & 0 \\ 0 & 0 & -1 \end{pmatrix}. \tag{2.3}$$

To gain further insight into the spin-spin coupling term, we write it explicitly as

$$2\hat{\Psi}_0^\dagger\hat{\Psi}_0^\dagger\hat{\Psi}_1\hat{\Psi}_{-1} + 2\hat{\Psi}_0\hat{\Psi}_0\hat{\Psi}_1^\dagger\hat{\Psi}_{-1}^\dagger + 2\hat{n}_0\left(\hat{n}_1 + \hat{n}_{-1}\right) + \left(\hat{n}_1 - \hat{n}_{-1}\right)^2, \tag{2.4}$$

where $\hat{n}_m = |\hat{\Psi}_m|^2$ is the density operator of the mth component. The first two terms describe spin-changing collisions (SCC) [2], i.e. two atoms in the $m_F = 0$ component get annihilated and a pair of atoms in the $m_F = \pm 1$ components is created or vice versa. The detuning of this process is given by the quadratic Zeeman energy q. The third term leads to an energy shift proportional to the population and the last one gives rise to spin-z domain formation for $c_1 < 0$.
In the meanfield description, which introduces the order parameter $\psi_m = \left\langle \hat{\Psi}_m \right\rangle$, we write the action neglecting quantum fluctuations as

$$\begin{aligned} S = \int \mathrm{d}t\, \mathrm{d}\vec{r} \Bigg[& \psi_m^* \left(i\hbar\frac{\partial}{\partial t} + \frac{\hbar^2}{2M}\nabla^2 - V_{\mathrm{ext}} \right) \psi_m - \psi_m^* q \left(f_z^2\right)_{ml} \psi_l \\ & - \frac{c_0}{2}\psi_m^*\psi_l^*\psi_l\psi_m - \frac{c_1}{2}\psi_l^*\psi_j^* \left(f_\alpha\right)_{jk} \left(f_\alpha\right)_{lm} \psi_k\psi_m \Bigg]. \end{aligned} \tag{2.5}$$

In the experiment, the atoms are confined in a longitudinal cigar-shaped trap with the trapping potential given by

$$V_{\mathrm{ext}}(\vec{r}) = \frac{1}{2}M\omega_\parallel^2 x^2 + \frac{1}{2}M\omega_\perp^2 r_\perp^2, \tag{2.6}$$

where $\omega_\parallel = \omega_x$ is the longitudinal and $\omega_\perp = \omega_y = \omega_z$ is the transversal trapping frequency with $\omega_\parallel \ll \omega_\perp$.

2.1.2 Quasi 1D action functional

To derive the quasi one-dimensional action functional, we factorize the wave function into a transversal and longitudinal part as

$$\psi_m(\vec{r}, t) = \psi_\perp(\vec{r}_\perp, \sigma(x,t))\psi_m(x,t), \tag{2.7}$$

with the variational functions $\sigma(x,t)$ and $\psi_m(x,t)$. The transversal wave function is equal for all three components and satisfies $\int \mathrm{d}\vec{r}_\perp |\psi_\perp|^2 = 1$. We further assume that it has a weak time and x dependence such that $\partial\psi_\perp/\partial t \simeq 0$ and $\nabla^2\psi_\perp \simeq \nabla_\perp^2\psi_\perp$.
Inserting equation (2.7) into equation (2.5), yields the effective quasi one-dimensional

action functional

$$S = \int \mathrm{d}t\,\mathrm{d}x \left[\psi_m^* \left(i\hbar\frac{\partial}{\partial t} + \frac{\hbar^2}{2M}\frac{\partial^2}{\partial x^2} - \frac{1}{2}M\omega_\parallel^2 x^2 - E_\perp(\sigma) \right) \psi_m \right.$$
$$-\psi_m^* q \left(f_z^2\right)_{ml} \psi_l - \chi(\sigma)\frac{c_0}{2}\psi_m^*\psi_l^*\psi_l\psi_m$$
$$\left. -\chi(\sigma)\frac{c_1}{2}\psi_l^*\psi_j^* \left(f_\alpha\right)_{jk}\left(f_\alpha\right)_{lm}\psi_k\psi_m \right]. \tag{2.8}$$

Here, $\psi_m \equiv \psi_m(x,t)$, $E_\perp(\sigma) = \int \mathrm{d}\vec{r}_\perp \psi_\perp^* \left[-\frac{\hbar^2}{2M}\nabla_\perp^2 + \frac{1}{2}M\omega_\perp^2 r_\perp^2 \right] \psi_\perp$ is the transversal mode energy and $\chi(\sigma) = \int \mathrm{d}\vec{r}_\perp |\psi_\perp|^4$ is the scaling factor of the nonlinear interaction.

2.1.3 Equations of motion

Applying the least action principle to equation (2.8) and inserting the spin-1 matrices stated in equation (2.3), we obtain the following equations of motion

$$i\hbar\frac{\partial}{\partial t}\psi_1 = \left[-\frac{\hbar^2}{2M}\frac{\partial^2}{\partial x^2} + \frac{1}{2}M\omega_\parallel^2 x^2 + q + E_\perp + \chi c_0 n + \chi c_1 \left(n_1 + n_0 - n_{-1}\right) \right] \psi_1$$
$$+ \chi c_1 \psi_0^2 \psi_{-1}^*, \tag{2.9}$$
$$i\hbar\frac{\partial}{\partial t}\psi_0 = \left[-\frac{\hbar^2}{2M}\frac{\partial^2}{\partial x^2} + \frac{1}{2}M\omega_\parallel^2 x^2 + E_\perp + \chi c_0 n + \chi c_1 \left(n_1 + n_{-1}\right) \right] \psi_0$$
$$+ 2\chi c_1 \psi_1 \psi_{-1} \psi_0^*, \tag{2.10}$$
$$i\hbar\frac{\partial}{\partial t}\psi_{-1} = \left[-\frac{\hbar^2}{2M}\frac{\partial^2}{\partial x^2} + \frac{1}{2}M\omega_\parallel^2 x^2 + q + E_\perp + \chi c_0 n + \chi c_1 \left(n_{-1} + n_0 - n_1\right) \right] \psi_{-1}$$
$$+ \chi c_1 \psi_0^2 \psi_1^*, \tag{2.11}$$
$$n\frac{\partial E_\perp}{\partial \sigma} + \left(\frac{c_0}{2}n^2 + \frac{c_1}{2}S \right) \frac{\partial \chi}{\partial \sigma} = 0, \tag{2.12}$$

where $S = 2\psi_0^*\psi_0^*\psi_1\psi_{-1} + 2\psi_0\psi_0\psi_1^*\psi_{-1}^* + 2n_0\left(n_1 + n_{-1}\right) + \left(n_1 - n_{-1}\right)^2$ contains the spin terms, $n_m = |\psi_m|^2$ is the density of the mth component, and $n = \sum_m n_m$ is the total density.

As in our case $\mu - E_\perp \simeq \hbar\omega_\perp$, we use a Gaussian function with width σ as an Ansatz for the transversal wave function in equation (2.7)

$$\psi_\perp(\vec{r}_\perp, \sigma(x,t)) = \frac{1}{\sqrt{\pi}\sigma}\exp\left[-\frac{r_\perp^2}{2\sigma^2} \right]. \tag{2.13}$$

Gross-Pitaevskii equation

In a strictly one-dimensional setting, the system is transversally in the ground state, i.e. the width of the Gaussian function is fixed to $\sigma(x,t) \equiv \sigma = a_\perp$ with the transversal oscillator length $a_\perp = \sqrt{\hbar/M\omega_\perp}$. The corresponding transversal mode energy and the scaling factor of the non-linear interaction (see equation (2.8)) read

$$E_\perp = \hbar\omega_\perp, \tag{2.14}$$

$$\chi = \frac{1}{2\pi a_\perp^2}. \tag{2.15}$$

Omitting the additive constant $E_\perp$, which does not affect the dynamics, we obtain the one-dimensional Gross-Pitaevskii equations (GPE)

$$\begin{aligned} i\hbar\frac{\partial}{\partial t}\psi_1 = &\left[-\frac{\hbar^2}{2M}\frac{\partial^2}{\partial x^2} + \frac{1}{2}M\omega_\parallel^2 x^2 + q + c_0^{1\mathrm{D}} n + c_1^{1\mathrm{D}}\left(n_1 + n_0 - n_{-1}\right)\right]\psi_1 \\ &+ c_1^{1\mathrm{D}}\psi_0^2\psi_{-1}^*, \end{aligned} \tag{2.16}$$

$$\begin{aligned} i\hbar\frac{\partial}{\partial t}\psi_0 = &\left[-\frac{\hbar^2}{2M}\frac{\partial^2}{\partial x^2} + \frac{1}{2}M\omega_\parallel^2 x^2 + c_0^{1\mathrm{D}} n + c_1^{1\mathrm{D}}\left(n_1 + n_{-1}\right)\right]\psi_0 \\ &+ 2c_1^{1\mathrm{D}}\psi_1\psi_{-1}\psi_0^*, \end{aligned} \tag{2.17}$$

$$\begin{aligned} i\hbar\frac{\partial}{\partial t}\psi_{-1} = &\left[-\frac{\hbar^2}{2M}\frac{\partial^2}{\partial x^2} + \frac{1}{2}M\omega_\parallel^2 x^2 + q + c_0^{1\mathrm{D}} n + c_1^{1\mathrm{D}}\left(n_{-1} + n_0 - n_1\right)\right]\psi_{-1} \\ &+ c_1^{1\mathrm{D}}\psi_0^2\psi_1^*. \end{aligned} \tag{2.18}$$

The one-dimensional couplings are given in terms of the three-dimensional ones by

$$c_0^{1\mathrm{D}} = \frac{c_0}{2\pi a_\perp^2}, \qquad c_1^{1\mathrm{D}} = \frac{c_1}{2\pi a_\perp^2}. \tag{2.19}$$

Non-polynomial Schrödinger equation

Allowing for transversal excitations in the system by using a variable width $\sigma(x,t)$ in equation (2.13), leads to the quasi one-dimensional description of the dynamics. In terms of the transversal oscillator length $a_\perp$, the transversal mode energy and the scaling factor

of the non-linear interaction (see equation (2.8)) read

$$E_\perp = \frac{\hbar\omega_\perp}{2}\left(\frac{a_\perp^2}{\sigma^2} + \frac{\sigma^2}{a_\perp^2}\right), \tag{2.20}$$

$$\chi = \frac{1}{2\pi\sigma^2}. \tag{2.21}$$

Plugging the results into equation (2.12) and solving for the width σ leads to

$$\sigma^2 = a_\perp^2\sqrt{1 + 2\left(\tilde{a}_0 n + \tilde{a}_1\frac{S}{n}\right)} \equiv a_\perp^2\sqrt{\kappa}, \tag{2.22}$$

where $\tilde{a}_0 = \frac{a_0+2a_2}{3}$ and $\tilde{a}_1 = \frac{a_2-a_0}{3}$ are the effective scattering lengths deduced from the couplings c_0 and c_1.
With this, we finally arrive at the non-polynomial Schrödinger equations (NPSE)

$$\begin{aligned} i\hbar\frac{\partial}{\partial t}\psi_1 = &\left[-\frac{\hbar^2}{2M}\frac{\partial^2}{\partial x^2} + \frac{1}{2}M\omega_\parallel^2 x^2 + q + E_\perp + \frac{c_0^{1\mathrm{D}}}{\sqrt{\kappa}}n + \frac{c_1^{1\mathrm{D}}}{\sqrt{\kappa}}\left(n_1 + n_0 - n_{-1}\right)\right]\psi_1 \\ &+ \frac{c_1^{1\mathrm{D}}}{\sqrt{\kappa}}\psi_0^2\psi_{-1}^*, \end{aligned} \tag{2.23}$$

$$\begin{aligned} i\hbar\frac{\partial}{\partial t}\psi_0 = &\left[-\frac{\hbar^2}{2M}\frac{\partial^2}{\partial x^2} + \frac{1}{2}M\omega_\parallel^2 x^2 + E_\perp + \frac{c_0^{1\mathrm{D}}}{\sqrt{\kappa}}n + \frac{c_1^{1\mathrm{D}}}{\sqrt{\kappa}}\left(n_1 + n_{-1}\right)\right]\psi_0 \\ &+ 2\frac{c_1^{1\mathrm{D}}}{\sqrt{\kappa}}\psi_1\psi_{-1}\psi_0^*, \end{aligned} \tag{2.24}$$

$$\begin{aligned} i\hbar\frac{\partial}{\partial t}\psi_{-1} = &\left[-\frac{\hbar^2}{2M}\frac{\partial^2}{\partial x^2} + \frac{1}{2}M\omega_\parallel^2 x^2 + q + E_\perp + \frac{c_0^{1\mathrm{D}}}{\sqrt{\kappa}}n + \frac{c_1^{1\mathrm{D}}}{\sqrt{\kappa}}\left(n_{-1} + n_0 - n_1\right)\right]\psi_{-1} \\ &+ \frac{c_1^{1\mathrm{D}}}{\sqrt{\kappa}}\psi_0^2\psi_1^*, \end{aligned} \tag{2.25}$$

where the transversal mode energy is given by $E_\perp = \frac{\hbar\omega_\perp}{2}\left(\frac{1}{\sqrt{\kappa}} + \sqrt{\kappa}\right)$.
Since the correction factor $1/\sqrt{\kappa}$ leads to a non-polynomial structure of the equations of motion, they are referred to as non-polynomial Schrödinger equations. Taking the expression for the correction factor from equation (2.22), we observe that it depends locally on the total density n and the spin term S. This gives rise to local corrections to the couplings which affect the dynamics in a trapped system, where the density is inhomogeneous.

2.2 Effective spin-1 description

Going over to an effective spin-1 system, which describes the experiment, the interaction couplings c_0 and c_1 have to be adjusted. For the hyperfine manifold $F = 2$ the interaction part of the action reads [6]

$$\begin{aligned} &- \frac{c_0^{\mathrm{F}=2}}{2}\psi_m^*\psi_l^*\psi_l\psi_m - \frac{c_1^{\mathrm{F}=2}}{2}\psi_l^*\psi_j^*\left(f_\alpha^{\mathrm{F}=2}\right)_{jk}\left(f_\alpha^{\mathrm{F}=2}\right)_{lm}\psi_k\psi_m \\ &- \frac{c_2^{\mathrm{F}=2}}{2}\frac{1}{5}\left[(-1)^{2-m}\psi_m^*\psi_{-m}^*\right]\left[(-1)^{2-l}\psi_l\psi_{-l}\right], \end{aligned} \tag{2.26}$$

where $f_\alpha^{\mathrm{F}=2}$ are the spin-2 matrices, $m = \pm 2, \pm 1, 0$ denotes the five magnetic sublevels of the $F = 2$ manifold and the couplings are given by

$$c_0^{\mathrm{F}=2} = \frac{4g_2 + 3g_4}{7}, \quad c_1^{\mathrm{F}=2} = \frac{g_4 - g_2}{7}, \quad c_2^{\mathrm{F}=2} = \frac{7g_0 - 10g_2 + 3g_4}{7}. \tag{2.27}$$

Neglecting terms containing contributions from the $m_F = \pm 2$ components and rearranging the remaining ones in the form displayed in equation (2.5), we obtain the effective spin-1 interaction part

$$- \frac{c_0^{\mathrm{eff}}}{2}\psi_m^*\psi_l^*\psi_l\psi_m - \frac{c_1^{\mathrm{eff}}}{2}\psi_l^*\psi_j^*\left(f_\alpha\right)_{jk}\left(f_\alpha\right)_{lm}\psi_k\psi_m, \tag{2.28}$$

where $m = \pm 1, 0$ denotes again the three sublevels of the $F = 1$ manifold, f_α are the spin-1 matrices and the effective couplings read

$$c_0^{\mathrm{eff}} = c_0^{\mathrm{F}=2} + \frac{c_2^{\mathrm{F}=2}}{5} = \frac{7g_0 + 10g_2 + 18g_4}{35}, \tag{2.29}$$

$$c_1^{\mathrm{eff}} = 3c_1^{\mathrm{F}=2} - \frac{c_2^{\mathrm{F}=2}}{5} = \frac{12\left(g_4 - g_2\right) + 7\left(g_2 - g_0\right)}{35}. \tag{2.30}$$

As $c_2^{\mathrm{F}=2}$ is a small contribution, we find that in the effective spin-1 description the density-density coupling just changes slightly corresponding to the $F = 2$ value. However, the spin-spin coupling is about three times larger, which leads to a different timescale for the emergence of spin structures during the time evolution.

In section 4.1 we apply equation (2.29) and (2.30) to calculate the couplings for the experimental parameter set. After converting them into the associated one-dimensional quantities with equation (2.19), we use the effective couplings in the equations of motion to perform simulations in a strictly one-dimensional setting (equations (2.16) - (2.18)), where the system is transversally in the ground state, as well as in the quasi

one-dimensional regime (equations (2.23) - (2.25)), where we allow for transversal excitations in the system.

2.3 Phase diagram

To obtain the phase diagram of the effective spin-1 Bose gas, we first calculate the meanfield ground states of the system. Starting from equation (2.5), the meanfield energy functional is

$$\mathcal{E} = \int \mathrm{d}\vec{r} \Bigg[\psi_m^* \left(-\frac{\hbar^2}{2M}\nabla^2 + V_{\mathrm{ext}} \right) \psi_m + \psi_m^* q \left(f_z^2\right)_{ml} \psi_l + \frac{c_0}{2}\psi_m^*\psi_l^*\psi_l\psi_m + \frac{c_1}{2}\psi_l^*\psi_j^* \left(f_\alpha\right)_{jk} \left(f_\alpha\right)_{lm} \psi_k\psi_m \Bigg]. \tag{2.31}$$

We consider a uniform system with fixed number density n and write

$$\psi_m = \sqrt{n}\zeta_m, \tag{2.32}$$

where we have introduced a normalized spinor ζ_m. In this notation the energy per particle, neglecting the kinetic term and the external potential, can be written as [6]

$$\varepsilon = \sum_m q m^2 |\zeta_m|^2 + \frac{1}{2}c_0 n + \frac{1}{2}c_1 n |\mathbf{f}|^2, \tag{2.33}$$

with the spin expectation value per particle $\mathbf{f} = \zeta_m^* \left(\boldsymbol{f}\right)_{ml} \zeta_l$.
Since $c_1 > 0$ in the effective description of the experimental system, we only discuss this part of the phase diagram. For $q > 0$ the energy per particle is minimized by the polar state $\psi \sim (0,1,0)^T$, whereas in the case $q < 0$, the system is in the paramagnetic phase where the ground state is $\psi \sim (1,0,1)^T$. Both have zero mean magnetization. The corresponding phase diagram is shown in Fig. 2.1. We study non-equilibrium dynamics by performing a sudden quench of the magnetic field, which is proportional to the quadratic Zeeman energy q, from the polar into the paramagnetic phase. By means of the quench, instabilities are triggered in the system as the initially prepared polar state is not the ground state anymore.
To get predictions for the resulting short time dynamics of the system, we consider small fluctuations around the initial meanfield ground state in the polar phase. To calculate the underlying excitations of the system, we apply Bogoliubov theory.

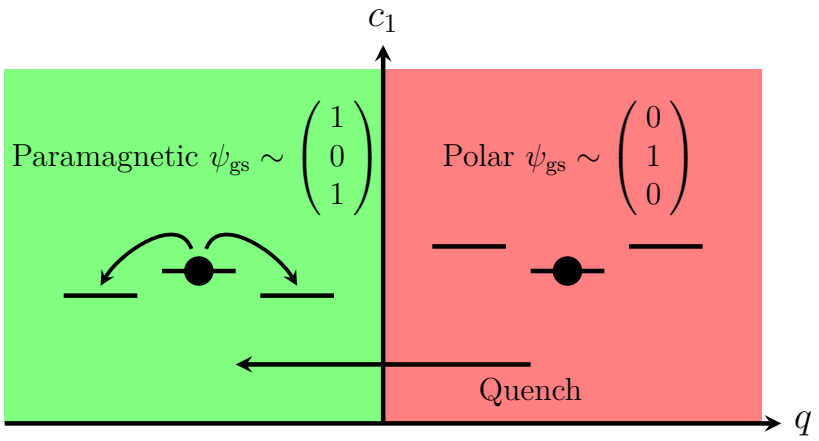

Figure 2.1: Phase diagram of the meanfield ground states in the effective spin-1 system with $c_1 > 0$. For the quadratic Zeeman energy $q > 0$ (red area) the system is in the polar phase, whereas for $q < 0$ (green area) it is in the paramagnetic phase. The phase transition in between is of first order. For each phase the single particle energy level scheme of the three magnetic sublevels is depicted. Quenching the magnetic field, which is proportional to the quadratic Zeeman energy, from the polar into the paramagnetic phase allows for spin-changing collisions as the side modes are energetically lowered.

2.4 Bogoliubov theory

The dynamics on short timescales, where we only have small fluctuations around the above discussed meanfield ground state, is expected to be described by Bogoliubov theory. Therefore we expand the Hamiltonian of the system up to second order in the fluctuations. Then we perform a Bogoliubov transformation in order to diagonalise the resulting Hamiltonian. This procedure leads to the energy spectra of the excitations in the system which allow for identifying unstable modes. In the following we only briefly review the important steps of the calculation done in a spatially homogeneous system, where we get analytical expressions for the energy spectra. A detailed derivation can be found in [6] and [18]. At the end of this section we discuss the applicability of the homogeneous Bogoliubov theory for the trapped system we are looking at in this thesis. We consider a spatially homogeneous system by setting the external potential to zero. We expand the field operators into plane waves as

$$\hat{\Psi}_m = \frac{1}{\sqrt{\Omega}} \sum_k \hat{a}_{k,m} e^{ikx}, \tag{2.34}$$

where Ω is the volume of the system and $\hat{a}_{k,m}$ is the Bosonic annihilation operator in mode k and magnetic sublevel m.
To expand the Hamiltonian up to second order in the fluctuations, we perform the following steps:

1. Insert the plane wave expansion into the one-dimensional Hamiltonian

$$\hat{H} = \int \mathrm{d}x \left[\hat{\Psi}_m^\dagger \left(-\frac{\hbar^2}{2M} \frac{\partial^2}{\partial x^2} \right) \hat{\Psi}_m + \hat{\Psi}_m^\dagger q \left(f_z^2 \right)_{ml} \hat{\Psi}_l + \frac{c_0}{2} \hat{\Psi}_m^\dagger \hat{\Psi}_l^\dagger \hat{\Psi}_l \hat{\Psi}_m + \frac{c_1}{2} \hat{\Psi}_l^\dagger \hat{\Psi}_j^\dagger \left(f_\alpha \right)_{jk} \left(f_\alpha \right)_{lm} \hat{\Psi}_k \hat{\Psi}_m \right]. \tag{2.35}$$

2. Perform the integration over the spatial coordinate x by introducing the relation $\delta_{k,k'} = \frac{1}{\Omega} \int \mathrm{d}x \, e^{i(k-k')x}$. Use this relation, which is a momentum conservation condition, to eliminate one of the Fourier sums in the Hamiltonian.

3. Replace the operator $\hat{a}_{0,0}^{(\dagger)}$ by a c-number $\sqrt{N}$ (with total atom number N) since the $k = 0$ mode in the $m_F = 0$ component is macroscopically occupied in the initial Bose-condensed state in the polar phase. This is only valid in the limit of small depletion. All other operators $\hat{a}_{k\neq 0,m}^{(\dagger)}$ are retained up to second order in the Hamiltonian.

4. Introduce operators which describe the fluctuations in transversal spin direction

$$\hat{a}_{k,f_x} = \frac{1}{\sqrt{2}} \left(\hat{a}_{k,1} + \hat{a}_{k,-1} \right), \qquad \hat{a}_{k,f_y} = \frac{i}{\sqrt{2}} \left(\hat{a}_{k,1} - \hat{a}_{k,-1} \right). \tag{2.36}$$

We end up with [6]

$$\hat{H}^{(2)} = \frac{\Omega n^2 c_0}{2} + \sum_{k\neq 0} \left[\left(\epsilon_k + n c_0 \right) \hat{a}_{k,0}^\dagger \hat{a}_{k,0} + \frac{n c_0}{2} \left(\hat{a}_{k,0}^\dagger \hat{a}_{-k,0}^\dagger + \hat{a}_{k,0} \hat{a}_{-k,0} \right) + \sum_{f=f_x,f_y} \left\{ \left(\epsilon_k + q + n c_1 \right) \hat{a}_{k,f}^\dagger \hat{a}_{k,f} + \frac{n c_1}{2} \left(\hat{a}_{k,f}^\dagger \hat{a}_{-k,f}^\dagger + \hat{a}_{k,f} \hat{a}_{-k,f} \right) \right\} \right], \tag{2.37}$$

where $\epsilon_k = \hbar^2 k^2 / 2M$ and $n = N/\Omega$ denotes the particle density.

By means of a Bogoliubov transformation with

$$\hat{b}_{k,0} = \sqrt{\frac{\epsilon_k + nc_0 + \omega_{k,0}}{2\omega_{k,0}}}\hat{a}_{k,0} + \sqrt{\frac{\epsilon_k + nc_0 - \omega_{k,0}}{2\omega_{k,0}}}\hat{a}^\dagger_{-k,0}, \tag{2.38}$$

$$\hat{b}_{k,f} = \sqrt{\frac{\epsilon_k + q + nc_1 + \omega_{k,f}}{2\omega_{k,f}}}\hat{a}_{k,f} + \sqrt{\frac{\epsilon_k + q + nc_1 - \omega_{k,f}}{2\omega_{k,f}}}\hat{a}^\dagger_{-k,f}, \tag{2.39}$$

where $f = f_{x,y}$, the diagonalized Hamiltonian reads

$$\hat{H}^{(2)} = \sum_{k\neq 0}\left[\omega_{k,0}\hat{b}^\dagger_{k,0}\hat{b}_{k,0} + \omega_{k,f_x}\hat{b}^\dagger_{k,f_x}\hat{b}_{k,f_x} + \omega_{k,f_y}\hat{b}^\dagger_{k,f_y}\hat{b}_{k,f_y}\right] + \text{const.} \tag{2.40}$$

The eigenenergies of the modes are given by

$$\omega^2_{k,0} = \epsilon_k\left(\epsilon_k + 2nc_0\right), \tag{2.41}$$

$$\omega^2_{k,f} = \left(\epsilon_k + q\right)\left(\epsilon_k + q + 2nc_1\right). \tag{2.42}$$

As the time evolution of such modes is proportional to $e^{-i\omega_k t/\hbar}$, imaginary eigenenergies, respectively $\omega_k^2 < 0$, lead to exponential growth of the corresponding modes.
Both dispersion relations normalized to the spin interaction strength nc_1 are depicted in Fig. 2.2. The dispersion given by equation (2.41) is gapless and has no unstable modes. It describes density excitations in the system. In contrast, the degenerate spectra of the transversal spin excitations (equation (2.42)) exhibit unstable modes for $q < 0$. Depending on the magnitude of q compared to nc_1, there are three different instability regions. Each spectrum of the transversal spin excitations in Fig. 2.2 belongs to one of these regions. Their upper momentum bound is given by $k_{\text{ub}} = \sqrt{2Mq/\hbar^2}$. In case of $-q > 2nc_1$, the lower k modes are no longer unstable which give rise to an additional lower bound of the instability region. The most unstable mode, which corresponds to the minimum of ω_f^2, is either

$$k_{\text{mu}} = 0 \qquad \text{for} \quad 0 < -q < nc_1, \tag{2.43}$$

or

$$k_{\text{mu}} = \sqrt{-2M\left(q + nc_1\right)/\hbar^2} \qquad \text{for} \quad -q > nc_1. \tag{2.44}$$

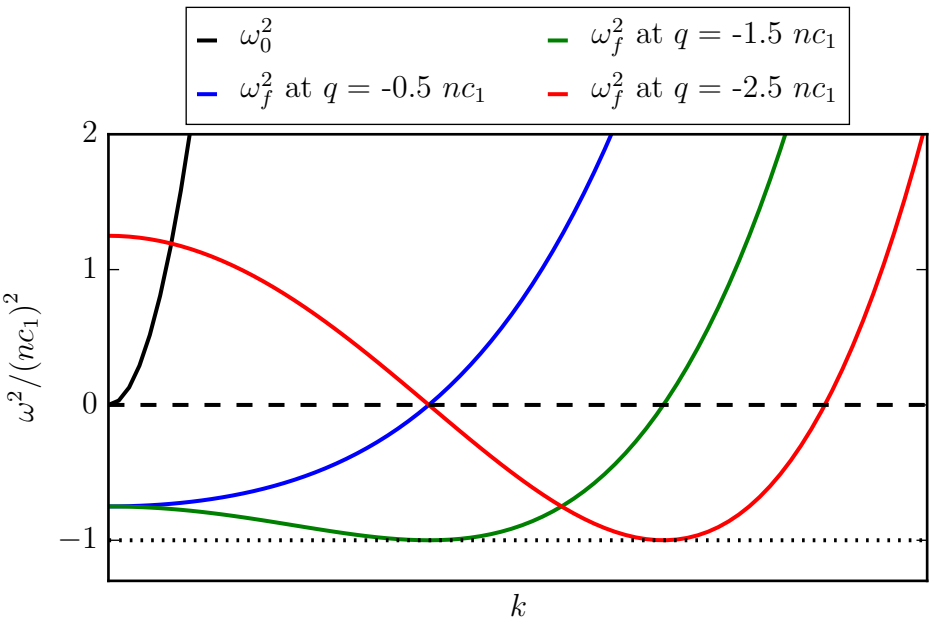

Figure 2.2: Bogoliubov dispersion relations for density excitations (ω_0^2) and transversal spin excitations (ω_f^2) normalized to nc_1. For values below the dashed line the corresponding momentum modes are unstable. The density excitation spectrum is gapless and has no unstable modes. The degenerate spectra of the transversal spin excitations exhibit unstable modes for $q < 0$. The coloured graphs illustrate the three different instability regions. The most unstable mode is either $k_{\mathrm{mu}} = 0$ for $0 < -q < nc_1$ (blue) or $k_{\mathrm{mu}} = \sqrt{-2M\left(q + 2nc_1\right)/\hbar^2}$ for $-q > nc_1$ (green, red). In case of $-q > 2nc_1$ (red), the lower k-modes are no longer unstable. The dotted line at $\omega = nc_1$ is related to the maximal growth rate of unstable modes.

The associated growth rates of the most unstable modes are given by

$$\gamma_{\mathrm{mu}} = \mathrm{Im}\left(\omega_{k_{\mathrm{mu},f}}\right) = \mathrm{Im}\left(\sqrt{q\left(q + 2nc_1\right)}\right) \qquad \text{for} \quad 0 < -q < nc_1, \tag{2.45}$$

$$\gamma_{\mathrm{mu}} = \mathrm{Im}\left(\omega_{k_{\mathrm{mu},f}}\right) = nc_1 \qquad \text{for} \quad -q > nc_1. \tag{2.46}$$

In section 4.2 we compare the predicted growth rates of unstable modes with simulations performed without external potential as a consistency check.

We expect the homogeneous Bogoliubov theory to be applicable for studying the most unstable momentum modes in the quench parameter regime $-q > nc_1$ in presence of a trapping potential because we are dealing with a many mode system due to a small longitudinal trapping frequency $\omega_{\parallel}$. In section 4.5 we show that the most unstable momentum modes extracted from numerical simulations performed in a trapping potential

are well described by the homogeneous Bogoliubov theory for $-q > nc_1$. For quench parameters in the regime $0 < -q < nc_1$ we expect deviations from the homogeneous prediction as there is no mode with zero momentum in the trap. In section 4.5 we indeed find that the emerging structure is related to the lowest momentum mode in the trap which is given by the extent of the condensate.

In this chapter we derived the equations of motion of a trapped effective spin-1 BEC in one spatial dimension. If the system is transversally in the ground state, the time evolution is given by the Gross-Pitaevskii equation (GPE). Allowing for excitations in the transversal trap direction leads to the quasi one-dimensional description of the system by means of the non-polynomial Schrödinger equation (NPSE). Performing simulations with both sets of equations of motion enable to identify if transversal excitations play a role in the experimental setup. As we later want to compare the short time dynamics of numerical simulations with experiments, we studied the homogeneous Bogoliubov theory, which gives analytical predictions for the emergence of structure on short timescales. We expect the homogeneous Bogoliubov theory to be applicable to our trapped system in the quench parameter regime $-q > nc_1$, whereas deviations in case of $0 < -q < nc_1$ are anticipated.
In the next chapter we set up the numerical framework for simulating the time evolution of a spin-1 Bose gas in one spatial dimension.

3 Simulation methods

In this chapter, we focus on the numerical tools and methods for simulating the time evolution of the above introduced equations of motion of a trapped (quasi) one-dimensional spin-1 Bose gas. We start with numerical basics involving the discretization of wave functions on a spatial grid and the adjustment of the corresponding momentum grid to resolve the relevant dynamical features. As we expect the important part of the dynamics to take place in the region of highly occupied modes, where it has been shown that the time evolution is well described by classical fields [8, 9, 10], we use the semi-classical Truncated Wigner Approximation (TWA). The method leads to approximative equations of motion for the Wigner function, which is the phase space representation of the density matrix. Instead of evolving the Wigner function in time, we propagate samples of classical fields whose initial probability distributions are given by the Wigner function. Physical quantities are obtained by averaging these samples. We find that the equations of motion for the fields within the TWA are the Gross-Pitaevskii equations for one-dimensional and the non-polynomial Schrödinger equations for quasi one-dimensional settings. The initial configuration of the fields is composed of the initial meanfield state of the system and quantum fluctuations which are sampled from the Wigner function of the vacuum. Thus the TWA allows for predictions beyond the meanfield approximation. At the end of this chapter we present two different approaches for sampling the quantum noise. To perform the time integration of the equations of motion obtained for the classical fields, we discuss the Fourier split-step method. For the construction of the initial field configuration we determine the initial meanfield state of the trapped system. As we want to start with the system being in the ground state of the polar phase in the harmonic trapping potential, we apply the concept of imaginary time propagation. This method asymptotically approaches the state of minimal energy of the trapped system.

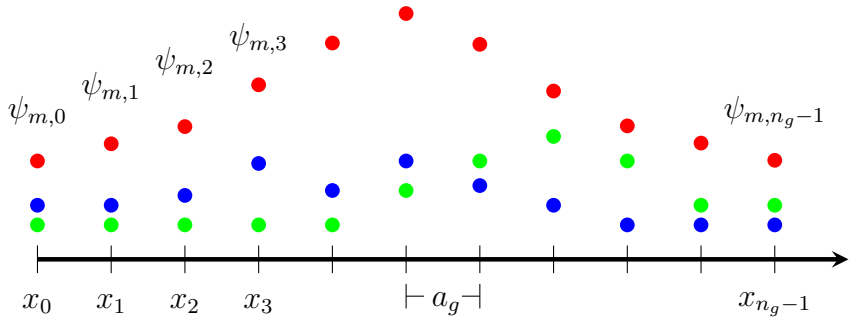

Figure 3.1: Discretization of the wave functions for the three components of a spin-1 BEC on a spatial grid with n_g grid points for a model setup. Each wave function, depicted by the red, blue and green dots, is associated to a vector of size n_g. The grid spacing a_g is given by the distance between two neighbouring grid points.

3.1 Basic numerical setup

Solving a set of equations of motion numerically requires a discretization of the involved wave functions on a spatial grid with n_g grid points. One model setup is schematically shown in Fig. 3.1. We associate the wave function for each of the three components to a vector of size n_g. The grid spacing a_g is given by the distance between two neighbouring grid points. In this thesis, we use a grid with $n_g = 16384 = 2^{14}$ grid points.
We express the equations of motion in terms of a length scale given by the grid spacing a_g and a corresponding time scale $\omega_g = \hbar/Ma_g^2$. We define the following rescaled variables

$$\bar{x} = \frac{x}{a_g}, \quad \bar{t} = \omega_g t, \quad \bar{c}_{0,1} = \frac{c_{0,1}}{\hbar\omega_g a_g}, \quad \bar{\omega}_{\parallel,\perp} = \frac{\omega_{\parallel,\perp}}{\omega_g}, \quad \bar{q} = \frac{q}{\hbar\omega}, \quad \bar{\psi} = \sqrt{a_g}\psi, \tag{3.1}$$

where quantities with a bar are dimensionless. The numerical resolvable real space features are thus solely determined by the choice of the length scale a_g. If we identify a_g with a physical spacing, the numerical quantities can be converted to physical ones.
By means of a Fourier transform we can directly assign a momentum grid to the above introduced spatial grid. To derive the lattice momenta we expand the fields into discrete plane waves. We insert this expansion into the expression for the discrete Laplacian on the spatial grid

$$\frac{\partial^2}{\partial x^2}\psi = \frac{\psi\left(x_{j+1}\right) - 2\psi\left(x_j\right) + \psi\left(x_{j-1}\right)}{a_g^2}, \tag{3.2}$$

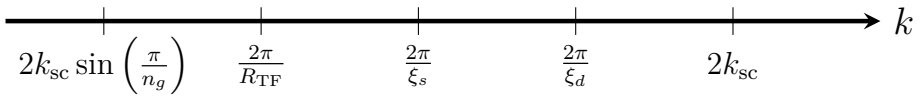

Figure 3.2: Adjustment of the momentum grid to resolve spin and density features as well as trap effects. The three momentum scales are associated with the spin healing length $\xi_s = \hbar/\sqrt{2Mnc_1}$, the density healing length $\xi_d = \hbar/\sqrt{2Mnc_0}$ and the Thomas-Fermi radius of the condensate $R_{\mathrm{TF}} = \sqrt{2\mu/M\omega_{\parallel}^2}$. The smallest non-zero mode $k_{\mathrm{min}} = 2k_{\mathrm{sc}} \sin\left(\frac{\pi}{n_g}\right)$ and the largest one $k_{\mathrm{max}} = 2k_{\mathrm{sc}}$ are tuned via the momentum scale factor k_{sc} such that they enclose all three scales. All quantities are expressed in terms of the inverse grid length a_g^{-1}.

which leads to the following relation for the lattice momenta

$$k_n = \frac{2}{a_g} \sin\left(\frac{\pi n}{n_g}\right), \tag{3.3}$$

with $n \in [-n_g/2 + 1, n_g/2]$. Due to our choice to take the discrete Laplacian, the lattice momenta are not linearly spaced. The spacing is denser in the ultra-violet (UV), whereas in the infra-red (IR) it is nearly linear. The maximal lattice momentum is $k_{\mathrm{max}} = 2/a_g$. It is convenient to set the resolution of the simulation by adjusting the UV and IR cutoff of the momentum grid. There are three characteristic momentum scales present, associated with the spin healing length $\xi_s = \hbar/\sqrt{2Mnc_1}$, the density healing length $\xi_d = \hbar/\sqrt{2Mnc_0}$ and the Thomas-Fermi radius of the condensate $R_{\mathrm{TF}} = \sqrt{2\mu/M\omega_{\parallel}^2}$. For a reasonable approximation of the dynamics, they have to be resolved on the momentum grid. Therefore we adjust the momenta such that they enclose all three scales. For that purpose we introduce a momentum scale factor k_{sc}, which modifies equation (3.3) to

$$k_n = \frac{2k_{\mathrm{sc}}}{a_g} \sin\left(\frac{\pi n}{n_g}\right). \tag{3.4}$$

We point out that, if $k_{\mathrm{sc}} \neq 1$, the inverse scaling has to be enforced on the spatial grid leading to a change in the length scale factor a_g. The adjustment of the momentum grid is illustrated in Fig. 3.2, where all quantities are expressed in terms of the inverse grid length a_g^{-1} for simplicity.

3.2 Truncated Wigner Approximation

As we expect the important part of the dynamics to take place in the region of highly occupied modes, we use the semi-classical Truncated Wigner method, which allows for predictions beyond the meanfield approximation as quantum noise is explicitly included in the initial state. We outline the method following [10, 11, 12, 13].
The first step is to construct a formulation of many-body quantum mechanics based on a phase space description. Therefore we start by introducing the Weyl symbol, which maps between quantum operators and ordinary functions in the phase space. In the coherent state representation of the phase space, the Weyl symbol for an arbitrary operator $\hat{A}\left(\hat{\boldsymbol{\psi}}, \hat{\boldsymbol{\psi}}^{\dagger}\right)$ is defined as

$$A_{\mathrm{W}}\left(\boldsymbol{\psi}, \boldsymbol{\psi}^{*}\right)=\iint \frac{\mathrm{d}\boldsymbol{\gamma}^{*}\,\mathrm{d}\boldsymbol{\gamma}}{2^{D}}\left\langle\boldsymbol{\psi}-\frac{\boldsymbol{\gamma}}{2}\right| \hat{A}\left(\hat{\boldsymbol{\psi}}, \hat{\boldsymbol{\psi}}^{\dagger}\right)\left|\boldsymbol{\psi}+\frac{\boldsymbol{\gamma}}{2}\right\rangle e^{-|\boldsymbol{\psi}|^{2}-\frac{1}{4}|\boldsymbol{\gamma}|^{2}} e^{\frac{1}{2}\left(\boldsymbol{\gamma}^{*} \boldsymbol{\psi}-\boldsymbol{\gamma} \boldsymbol{\psi}^{*}\right)}, \tag{3.5}$$

where $\boldsymbol{\psi}=\{\psi_m\}$ is the vector of the complex amplitudes of the magnetic sublevel states and D the size of the associated Hilbert space. The Weyl symbol of symmetrically ordered operators directly results from the substitution $\hat{\boldsymbol{\psi}}^{(\dagger)} \rightarrow \boldsymbol{\psi}^{(*)}$.
The Weyl symbol of the density matrix $\hat{\rho}$ is the Wigner function

$$W\left(\boldsymbol{\psi}, \boldsymbol{\psi}^{*}\right)=\iint \frac{\mathrm{d}\boldsymbol{\gamma}^{*}\,\mathrm{d}\boldsymbol{\gamma}}{2^{D}}\left\langle\boldsymbol{\psi}-\frac{\boldsymbol{\gamma}}{2}\right| \hat{\rho}\left(\hat{\boldsymbol{\psi}}, \hat{\boldsymbol{\psi}}^{\dagger}\right)\left|\boldsymbol{\psi}+\frac{\boldsymbol{\gamma}}{2}\right\rangle e^{-|\boldsymbol{\psi}|^{2}-\frac{1}{4}|\boldsymbol{\gamma}|^{2}} e^{\frac{1}{2}\left(\boldsymbol{\gamma}^{*} \boldsymbol{\psi}-\boldsymbol{\gamma} \boldsymbol{\psi}^{*}\right)}. \tag{3.6}$$

Using this mapping, the expectation value of any operator reads

$$\left\langle\hat{A}\left(\hat{\boldsymbol{\psi}}, \hat{\boldsymbol{\psi}}^{\dagger}\right)\right\rangle=\iint \mathrm{d}\boldsymbol{\psi}\,\mathrm{d}\boldsymbol{\psi}^{*} W\left(\boldsymbol{\psi}, \boldsymbol{\psi}^{*}\right) A_{\mathrm{W}}\left(\boldsymbol{\psi}, \boldsymbol{\psi}^{*}\right). \tag{3.7}$$

The Wigner function can be associated with a quasi-probability distribution, where the supplement quasi implies that it can become negative. However, in case of large occupation numbers, it can be treated as a classical probability distribution function.
The deduction of equations of motion requires the evaluation of operator products and commutators. Thus we will investigate the Weyl symbols of these objects.
As shown in [19], Weyl operators satisfy the so-called Moyal product relation given by

$$\left(A_1 A_2\right)_{\mathrm{W}}=A_{1,\mathrm{W}} \exp\left[\frac{\Lambda}{2}\right] A_{2,\mathrm{W}}, \tag{3.8}$$

with the symplectic operator

$$\Lambda = \sum_j \frac{\overleftarrow{\partial}}{\partial\psi_j}\frac{\overrightarrow{\partial}}{\partial\psi_j^*} - \frac{\overleftarrow{\partial}}{\partial\psi_j^*}\frac{\overrightarrow{\partial}}{\partial\psi_j}. \tag{3.9}$$

By direct application of the Moyal product relation to the commutator $\hat{A} = \left[\hat{A}_1, \hat{A}_2\right]$, one finds that its Weyl symbol is

$$A_{\mathrm{W}} = 2A_{1,\mathrm{W}} \sinh\left[\frac{\Lambda}{2}\right] A_{2,\mathrm{W}} = \{A_{1,\mathrm{W}}, A_{2,\mathrm{W}}\}_{\mathrm{MB}}\,. \tag{3.10}$$

$\{\dots\}_{\mathrm{MB}}$ denotes the Moyal bracket, which is defined as

$$\{\dots\}_{\mathrm{MB}} = 2\sinh\left[\frac{1}{2}\{\dots\}_{\mathrm{P}}\right], \tag{3.11}$$

with the classical Poisson bracket of two functions B and B' being

$$\{B, B'\}_{\mathrm{P}} = B\Lambda B' = \sum_j \frac{\partial B}{\partial\psi_j}\frac{\partial B'}{\partial\psi_j^*} - \frac{\partial B}{\partial\psi_j^*}\frac{\partial B'}{\partial\psi_j}. \tag{3.12}$$

With these relations at hand, we are able to derive the quantum equations of motion within the Truncated Wigner Approximation. We start with the von-Neumann equation for the many-body density matrix

$$i\hbar\frac{\partial\hat{\rho}}{\partial t} = \left[\hat{H}, \hat{\rho}\right]. \tag{3.13}$$

Performing the Weyl transformation on both sides of the equation and making use of equation (3.10) yields

$$i\hbar\frac{\partial W}{\partial t} = \{H_{\mathrm{W}}, W\}_{\mathrm{MB}} = 2H_{\mathrm{W}}\sinh\left[\frac{\Lambda}{2}\right] W, \tag{3.14}$$

where H_{W} is the Weyl ordered Hamiltonian of the system.
Expanding the equation up to third order in Λ leads to

$$i\hbar\frac{\partial W}{\partial t} = \{H_{\mathrm{W}}, W\}_{\mathrm{P}} + \frac{1}{8}\sum_{j,k,l}\frac{\partial^3 H_{\mathrm{W}}}{\partial\psi_j\partial\psi_k^*\partial\psi_l^*}\frac{\partial^3 W}{\partial\psi_j^*\partial\psi_k\partial\psi_l} - \frac{\partial^3 H_{\mathrm{W}}}{\partial\psi_j^*\partial\psi_k\partial\psi_l}\frac{\partial^3 W}{\partial\psi_j\partial\psi_k^*\partial\psi_l^*}. \tag{3.15}$$

The spin-1 Hamiltonian, introduced in equation (2.35), contains at most quartic terms in the fields $\hat{\psi}^{(\dagger)}$. Thus equation (3.15) is exact for our physical system. Because of the third-order derivatives, we have no method at hand to simulate the equation.
The simplest approximation is to truncate the expansion up to leading order in Λ, which goes under the name of the Truncated Wigner Approximation (TWA). Applying the TWA, we recover the classical Liouville equation for the density matrix

$$i\hbar\frac{\partial W}{\partial t} = \{H_{\mathrm{W}}, W\}_{\mathrm{P}}\,. \tag{3.16}$$

This partial differential equation can be solved by means of the method of characteristics [20].
We first briefly explain the general procedure of the method. For a more general transport equation given by

$$P(\psi,t)\frac{\partial W}{\partial t} + Q(\psi,t)\frac{\partial W}{\partial \psi} = 0, \tag{3.17}$$

a new variable τ is introduced, such that

$$\frac{\partial W}{\partial \tau} = 0. \tag{3.18}$$

The equations for the so-called characteristics then read

$$\frac{\partial t}{\partial \tau} = P\left(\psi(\tau), t(\tau)\right), \qquad \frac{\partial \psi}{\partial \tau} = Q\left(\psi(\tau), t(\tau)\right). \tag{3.19}$$

Comparing equations (3.17) and (3.16), it can be read off that $P(\psi,t) = i\hbar$ and $Q(\psi,t) = \partial H_W/\partial\psi^*$. Inserting these relations into equation (3.19) yields

$$i\hbar\frac{\partial \psi_m}{\partial t} = \frac{\partial H_W}{\partial \psi_m^*}, \tag{3.20}$$

where m denotes the three magnetic sublevels in the spin-1 description.
By using the Moyal product relation (equation (3.8)), one can straightforwardly show that Weyl ordering of the spin-1 Hamiltonian solely leads to additional terms proportional to the densities of the three sublevels $|\psi_m|^2$. The corresponding terms in the equations of motion (3.20) can be removed by a global gauge transformation such that the GPE (2.16 - 2.18) in the one-dimensional and the NPSE (2.23 - 2.25) in the quasi one-dimensional case are obtained.
Instead of evolving the Wigner function in time, we propagate samples of the classical

fields ψ_m whose initial probability distributions are given by the Wigner function. The initial configuration of the fields is composed of the initial meanfield state of the system and quantum fluctuations which are sampled from the Wigner function of the vacuum. Therefore effects of quantum noise are explicitly included via the initial state, although the equations are completely deterministic.
Equation (3.20) describes the trajectories of a single realisation of the classical fields ψ_m. If the Wigner function is positive definite, they might be associated with a single experimental run. Because of the stochastic nature of the quantum noise, physical quantities are obtained by averaging over many realisations. Different samplings of the initial quantum noise will be investigated in section 3.5.

3.3 Fourier split-step

To perform the time integration of the equations of motion for the classical fields, we utilise the particle number as well as total energy conserving split-step method [21]. In general, this method can be used to discretize the time variable for the numerical solution of non-linear Schrödinger-type equations.
To apply the scheme to our set of equations, we first write the equations of motion in matrix notation as

$$i\hbar\frac{\partial}{\partial t}\psi_m = \mathcal{H}_{ml}\psi_l, \tag{3.21}$$

where m and l label the three components.
$\mathcal{H}$ can be decomposed into a diagonal kinetic part and a part containing all other terms, including the nonlinear ones, which leads to

$$\mathcal{H}_{ml} = \mathcal{T}_{ml} + \mathcal{N}_{ml} = -\frac{\hbar^2}{2M}\frac{\partial^2}{\partial x^2}\delta_{ml} + \mathcal{N}_{ml}. \tag{3.22}$$

Advancing the solution to equation (3.21) at time t by a small time step Δt gives

$$\psi_m(x, t+\Delta t) = \left(e^{-\frac{i}{\hbar}\Delta t\mathcal{H}}\right)_{ml}\psi_l(x,t) = \left(e^{-\frac{i}{\hbar}\Delta t(\mathcal{T}+\mathcal{N})}\right)_{ml}\psi_l(x,t). \tag{3.23}$$

A simple time-splitting scheme, which makes use of the Baker-Campbell Hausdorff formula and is accurate to first order, is

$$\psi_m(x, t+\Delta t) = \left(e^{-\frac{i}{\hbar}\Delta t\mathcal{T}}\right)_{ml}\left(e^{-\frac{i}{\hbar}\Delta t\mathcal{N}}\right)_{lk}\psi_k(x,t) + \mathcal{O}\left(\Delta t^2\right). \tag{3.24}$$

The accuracy can be increased up to second order in time by splitting into three fractional steps as proposed in [22] and [23]. The final time integration scheme, which we utilise for our numerical simulations, is therefore

$$\psi_m(x,t+\Delta t) = \left(e^{-\frac{i}{\hbar}\frac{\Delta t}{2}\mathcal{T}}\right)_{ml}\left(e^{-\frac{i}{\hbar}\Delta t\mathcal{N}}\right)_{lk}\left(e^{-\frac{i}{\hbar}\frac{\Delta t}{2}\mathcal{T}}\right)_{kj}\psi_j(x,t) + \mathcal{O}\left(\Delta t^3\right). \tag{3.25}$$

The two matrix exponentials involving the kinetic part $\mathcal{T}$ can be easily calculated in Fourier space, where $\mathcal{T}_{ml} = \frac{\hbar^2k^2}{2M}\delta_{ml}$ is diagonal. Due to the performed Fourier transformations, the method is called Fourier or spectral split-step.
We are left over with the computation of the matrix exponential $\exp\left\{-\frac{i}{\hbar}\Delta t\mathcal{N}\right\}_{lk}$, which we carry out in real space. We use the Putzer algorithm [24] to explicitly calculate the matrix elements. The method and the obtained results for our spin-1 system are discussed in [25, 26].

3.4 Ground state via imaginary time propagation

Before performing the time evolution of the fields with the above introduced Fourier split-step method, we need to determine the initial configuration of the fields which are composed of the initial meanfield state of the system and quantum fluctuations which are sampled from the Wigner function of the vacuum. We first investigate the initial meanfield state of the system. As we want to perform a sudden parameter quench from the polar into the paramagnetic phase, we start with the system being in the ground state of the polar phase in the harmonic trapping potential.
One iterative method, which asymptotically approaches the state of minimal energy of the trapped system, is the imaginary time propagation (ITP). Expressing the wave function in terms of energy eigenstates as $\psi_m(x,t) = \sum_\lambda a_{m,\lambda}(t)\phi_{m,\lambda}(x)$ and going over to imaginary time $\tau = it$ by applying a Wick rotation to the time coordinate [27], equation (3.23) is modified to

$$\psi_m(x,\tau+\Delta\tau) = \sum_\lambda e^{-\frac{\Delta\tau}{\hbar}\mathrm{E}_{m,\lambda}}a_{m,\lambda}(\tau)\phi_{m,\lambda}(x), \tag{3.26}$$

where we do not sum over the component label m. The amplitudes of the eigenstates decay exponentially with a rate given by the corresponding eigenenergy. Therefore the state of minimal energy has the smallest damping, i.e. we end up with the system being in the ground state.

Due to the diffusive nature of the imaginary-time equations of motion, it is essential to rescale the wave function to the initial particle number after each time step. Otherwise the system does not converge to the correct ground state.
As we asymptotically reach the ground state, we need to formulate a convergence criterion to terminate the ITP. For our purpose, we stop the ITP if the difference between two wave function rescale factors, separated by 25 time steps, is smaller than $5 \cdot 10^{-10}$.

3.5 Noise sampling

After determining the initial meanfield state of the system, we need to additionally sample the quantum fluctuations from the Wigner function of the vacuum to construct the initial configurations of the fields.
We subsequently present two different approaches of noise sampling. In the first one the noise is set into Fourier modes up to a momentum cutoff, whereas in the second one the noise is sampled in the single particle eigenmodes of the effective potential for the $m_F = \pm 1$ components.

3.5.1 Fourier modes

In a homogeneous setup, i.e. without an external trapping potential, we expand the initial state into Fourier modes u as

$$\psi_m(x) = \sum_j u_{j,m}(x)\alpha_{j,m}, \tag{3.27}$$

where α_j are the mode coefficients. Some of these Fourier modes are occupied by the initial meanfield state of the system. We set quantum fluctuations into all unoccupied modes in all three components by means of complex Gaussian white noise with an average occupation number of half a particle per mode

$$\langle \alpha_{j,m} \rangle = \langle \alpha_{j,m}\alpha_{l,n} \rangle = 0, \qquad \left\langle \alpha^*_{j,m}\alpha_{l,n} \right\rangle = \frac{1}{2}\delta_{j,l}\delta_{m,n}. \tag{3.28}$$

Since the fraction of particles which are introduced via the noise should be small compared to the deterministic particles, we solely set noise into modes up to a momentum cutoff. We choose the cutoff such that all predicted unstable momentum modes (see section 2.4), which cause the structure formation on short timescales, are occupied with quantum noise. Thus we set quantum noise into modes up to twice the spin healing

momentum $k_{\xi_s} = 2\pi\sqrt{2Mnc_1}/\hbar$.
We expect that the Fourier modes are no longer suitable for the noise sampling, if we want to quantitatively compare simulations with experiments in presence of a trapping potential. As too many modes, that do not exist in the trapped system, are populated with quantum noise, the timescales of structure formation should change which we indeed find when comparing numerical simulations with experimental results in section 4.5.

3.5.2 Single particle eigenmodes of the effective potential

In this part, we focus on noise sampling in the $m_F = \pm 1$ components in presence of a trapping potential. The main goal is to find suitable eigenmodes of the trapped system with respect to the initial meanfield state of the system.
We present the derivation for the quasi one-dimensional case as this noise sampling is solely used in combination with NPSE simulations.
We start with the quasi one-dimensional spin-1 Hamiltonian

$$\begin{aligned} H = \int \mathrm{d}x \Bigg[& \psi_m^* \left(-\frac{\hbar^2}{2M}\frac{\partial^2}{\partial x^2} + V_{\mathrm{trap}}(x) + E_\perp \right) \psi_m \\ & + \psi_m^* q \left(f_z^2\right)_{ml} \psi_l + \frac{c_0}{2\sqrt{\kappa}} \psi_m^* \psi_l^* \psi_l \psi_m \\ & + \frac{c_1}{2\sqrt{\kappa}} \psi_l^* \psi_j^* \left(f_\alpha\right)_{jk} \left(f_\alpha\right)_{lm} \psi_k \psi_m \Bigg], \end{aligned} \tag{3.29}$$

where $E_\perp = \frac{\hbar\omega_\perp}{2}\left(\frac{1}{\sqrt{\kappa}} + \sqrt{\kappa}\right)$ is the transversal mode energy and $\sqrt{\kappa} = \sqrt{1 + 2\left(\tilde{a}_0 n + \tilde{a}_1 \frac{S}{n}\right)}$ the correction factor with the total density given by $n = \psi_m^* \psi_m$.
The subsequent derivation mainly follows [28]. For the initial state in the polar phase all atoms are in the $m_F = 0$ component. We make a Bogoliubov Ansatz by writing

$$\psi(x,t) = \left(\begin{pmatrix} 0 \\ \sqrt{n_0(x)} \\ 0 \end{pmatrix} + \begin{pmatrix} \delta\psi_1 \\ \delta\psi_0 \\ \delta\psi_{-1} \end{pmatrix} \right) e^{-i\mu t}, \tag{3.30}$$

where μ denotes the chemical potential and the fields $\delta\psi_m$ fluctuations of each component, which we consider to be small in the following.

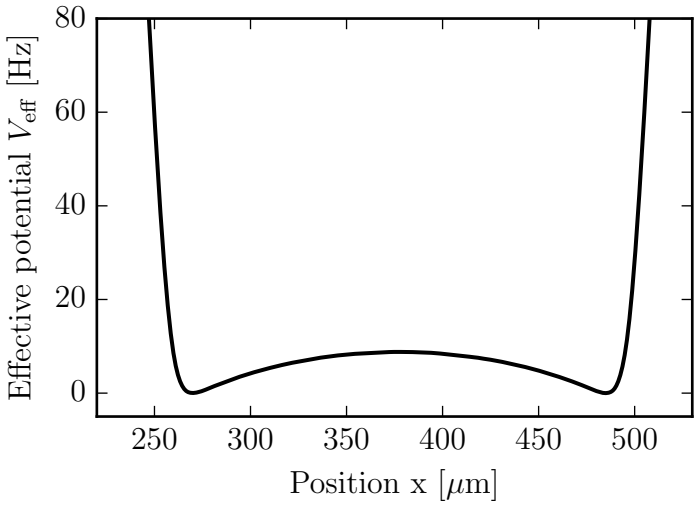

Figure 3.3: Effective potential V_{eff} for atoms in the $m_F = \pm 1$ components given by equation (3.33). Due to the repulsive interaction with atoms in the $m_F = 0$ component, the original harmonic trapping potential is modified.

Expanding the Hamiltonian up to second order in $\delta\psi_{\pm 1}$ leads to

$$\begin{aligned} H = \int \mathrm{d}x \Bigg[& \delta\psi_1^* \left(-\frac{\hbar^2}{2M}\frac{\partial^2}{\partial x^2} + V_{\text{trap}}(x) + \frac{(c_0 + c_1)\, n_0(x)}{\sqrt{1 + 2\tilde{a}_0 n_0(x)}} + \tilde{E}_\perp - \mu + q \right) \delta\psi_1 \\ & + \delta\psi_{-1}^* \left(-\frac{\hbar^2}{2M}\frac{\partial^2}{\partial x^2} + V_{\text{trap}}(x) + \frac{(c_0 + c_1)\, n_0(x)}{\sqrt{1 + 2\tilde{a}_0 n_0(x)}} + \tilde{E}_\perp - \mu + q \right) \delta\psi_{-1} \\ & + \frac{c_1 n_0(x)}{\sqrt{1 + 2\tilde{a}_0 n_0(x)}} \left(\delta\psi_1^* \delta\psi_{-1}^* + \delta\psi_1 \delta\psi_{-1} \right) \Bigg], \end{aligned} \tag{3.31}$$

where $\tilde{E}_\perp = \frac{\hbar\omega_\perp}{2}\left(1/\sqrt{1 + 2\tilde{a}_0 n_0(x)} + \sqrt{1 + 2\tilde{a}_0 n_0(x)}\right)$.
The single particle Hamiltonian for the $m_F = \pm 1$ components is given by

$$H_{\text{eff}} = -\frac{\hbar^2}{2M}\frac{\partial^2}{\partial x^2} + V_{\text{trap}}(x) + \frac{(c_0 + c_1)\, n_0(x)}{\sqrt{1 + 2\tilde{a}_0 n_0(x)}} + \tilde{E}_\perp - \mu, \tag{3.32}$$

such that the atoms feel the effective potential

$$V_{\text{eff}}(x) = V_{\text{trap}}(x) + \frac{(c_0 + c_1)\, n_0(x)}{\sqrt{1 + 2\tilde{a}_0 n_0(x)}} + \tilde{E}_\perp - \mu, \tag{3.33}$$

which is depicted in Fig. 3.3.

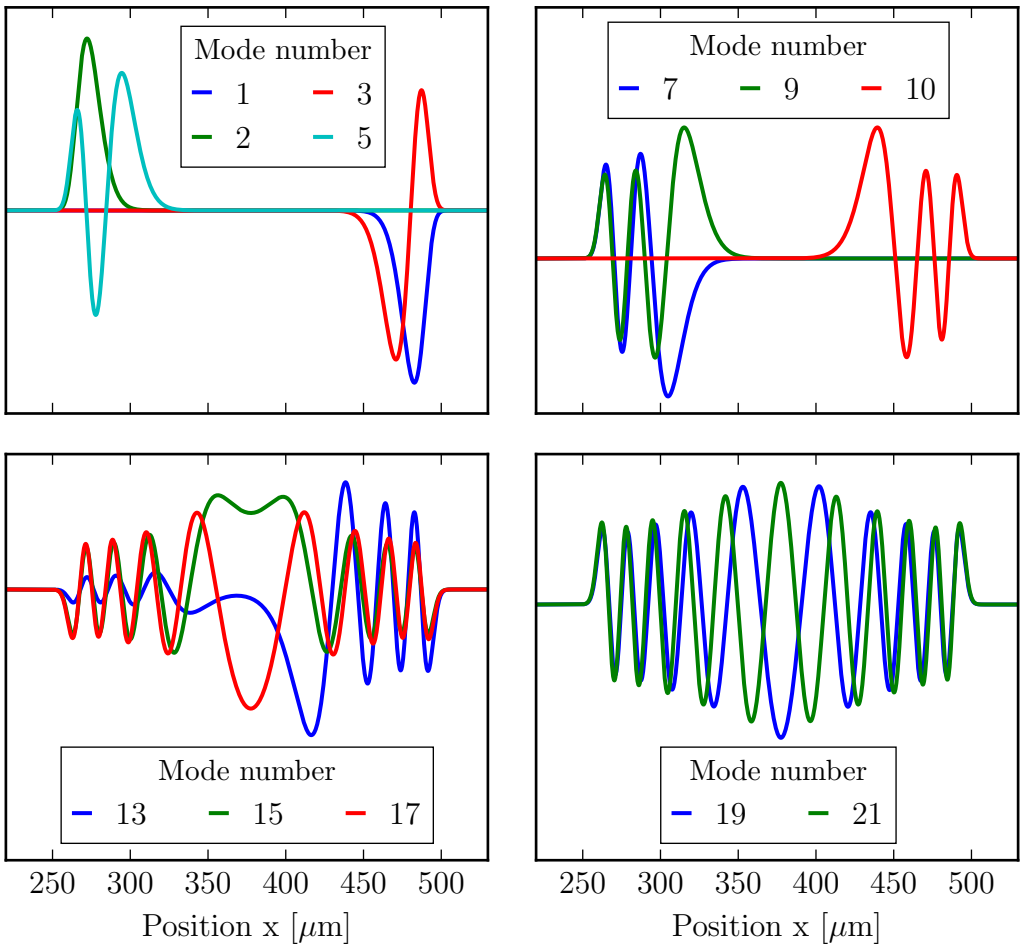

Figure 3.4: A variety of numerically calculated eigenmodes of the single particle Hamiltonian H_{eff}. We find that the energetically lowest modes are mainly located at the edges of the trap, whereas the energetically higher modes spread over the entire trap. As the modes are two-fold degenerate, we only set noise into every other of the eigenmodes starting with the energetically lowest one. To minimize the influence of noise particles, we choose the momentum cutoff to be slightly above the expected instability region. This corresponds to setting between five and ten noise particles on average into each of the $m_F = \pm 1$ components for quench parameters $-30\,\text{Hz} \leq q \leq -2\,\text{Hz}$. All depicted eigenmodes are normalized to one.

The initial state in the polar phase is prepared at a large positive value of the quadratic Zeeman energy q. Thus the $m_F = \pm 1$ states are empty and energetically tuned far away such that only the single particle Hamiltonian is relevant. To get an impression of how the single particle eigenmodes of the effective potential look like, a variety of numerically calculated eigenmodes of H_{eff} is shown in Fig. 3.4.

We expand the initial fields in the $m_F = \pm 1$ components in the single particle eigenmodes $u_{\pm 1}$ resulting in

$$\psi_{\pm 1}(x) = \sum_j u_{j,\pm 1}(x)\alpha_{j,\pm 1}, \tag{3.34}$$

where α_j are again the mode coefficients.
The quantum fluctuations are set according to equation (3.28). With regard to the eigenmodes displayed in Fig. 3.4, we find that the energetically lowest modes are mainly located at the edges of the trap. whereas the energetically higher modes spread over the entire trap. As the modes are two-fold degenerate, we only set noise into every other of the eigenmodes starting with the energetically lowest one. To minimize the influence of noise particles, we choose the momentum cutoff to be slightly above the expected instability region (see section 2.4). This corresponds to setting between five and ten noise particles on average into each of the $m_F = \pm 1$ components for quench parameters $-30\,\mathrm{Hz} \leq q \leq -2\,\mathrm{Hz}$. In [29] it has been shown that this procedure leads to an adequate description of experimental results.
So far we have only set quantum noise in the $m_F = \pm 1$ components. The additional sampling for the $m_F = 0$ component will be part of future work. It is referred to solving the Bogoliubov de-Gennes equations of a one component BEC and setting the initial noise into the calculated Bogoliubov modes [30]. Thus the initial field in the $m_F = 0$ component is solely given by the initial meanfield configuration.

In this chapter we introduced the semi-classical Truncated Wigner method, which allows for predictions beyond the meanfield approximation as quantum noise is explicitly included in the initial state. Instead of evolving the Wigner function in time, we propagate samples of classical fields whose initial probability distributions are given by the Wigner function. We found that the equations of motion for the classical fields within the Truncated Wigner approximation are the Gross-Pitaevskii equations for one-dimensional and the non-polynomial Schrödinger equations for quasi one-dimensional settings. The initial configuration of the fields is composed of the initial meanfield state of the system and quantum fluctuations which are sampled from the Wigner function of the vacuum. Thus we numerically determine the initial meanfield state in the harmonic trap, which is the ground state in the polar phase, by means of imaginary time propagation and sample the quantum noise into unoccupied modes up to a momentum cutoff. We calculated the single particle eigenmodes of the effective potential for the $m_F = \pm 1$ components to get a suitable noise sampling in presence of a trapping potential. Using the Fourier

split-step method we can perform the time integration of the equations of motion for the classical fields, which enables to study the dynamics of our system after performing a sudden parameter quench from the polar into the paramagnetic phase.
In the next chapter we investigate the emergence of structure in the system at short times after the sudden quench. We compare simulations performed with the two different noise samplings with experimental results. We find that it is indeed essential to set the initial quantum noise into the single particle eigenmodes of the effective potential for the $m_F = \pm 1$ components to recover the experimental dynamics.

4 Comparison of numerical simulations with experiments

In this chapter, we compare numerical simulations with experimental results. We focus on the emergence of structure at short times after a sudden parameter quench. We start with a brief description of the experimental setup. Then we discuss the relevant physical parameters, which are needed as an input for the simulation. To enable a quantitative comparison between numerical simulations and experiments, we first investigate whether transversal excitations are present in the experimental setup. If excitations in the transversal direction of the trap play a role in the experiment, the dynamics should be well described by the quasi one-dimensional equations of motion given by the non-polynomial Schrödinger equations (2.23) - (2.25). If the experimental system is transversally in the ground state, the one-dimensional equations of motion which are the Gross-Pitaevskii equations (2.16) - (2.18) should give results which fit to the experimentally observed dynamics. We find that the quasi one-dimensional description by means of the NPSE is the appropriate model to recover the experimental dynamics. As Bogoliubov excitations occur in the transversal spin direction, the transversal spin is a suited observable for analysing the dynamics on short time scales. Due to instabilities, which are triggered by the sudden quench, we observe spin domain formation in the transversal spin direction. The associated characteristic structure size of the system can be extracted from the minimum of the auto-correlation function of the transversal spin. We mimic the experimental measurement of the transversal spin by performing a $\pi/2$ rotation of the grid around a random axis in the x-y-plane of the spin-1 sphere. We then bin our data points such that they fit to the experimental imaging window and resolution. Finally, we add Gaussian white noise to model the experimental detection noise. With this at hand we are able to make a quantitative comparison between numerical simulations and experiments. Therefore we analyse the auto-correlation function and the corresponding Fourier spectra of the transversal spin for short evolution times. We present results of simulations performed with the two different noise samplings intro-

duced in section 3.5. We find that sampling the noise into the single particle eigenmodes of the effective potential for the $m_F = \pm 1$ components leads to good agreement of the structure size between simulation and experiment for some of the selected evolution times. Using the Fourier mode sampling the structure formation in the simulation is way faster than in the experiment. At the end of this chapter we compare NPSE simulations with the initial noise set into the single particle eigenmodes of the effective potential for the $m_F = \pm 1$ components to the homogeneous Bogoliubov theory. For short times we find that the structure size of the system follows the Bogoliubov prediction in the quench parameter regime $-q > nc_1$. For later times we expect deviations. However, we find that the structure size is again well described by Bogoliubov theory with a smaller spin interaction strength nc_1.

4.1 Experimental parameters

A major part of this chapter is concerned with comparing numerical simulations with experiments performed in the group of Prof. Dr. Markus K. Oberthaler. Therefore we briefly state the experimental parameters, which are needed as an input for the simulation. A detailed description of the experimental setup can be found in [14].
In the experiment, ^{87}Rb atoms are confined in a cigar-shaped trap with longitudinal trapping frequency $\omega_{\parallel} = 2\pi \cdot 2.6\,\mathrm{Hz}$ and transversal trapping frequency $\omega_{\perp} = 2\pi \cdot 260\,\mathrm{Hz}$. The atom number inside the analysis window ($120\,\mu$m around the centre of the trap) is between 24000 and 30000.
To calculate the coupling constants defined in equations (2.29) and (2.30), we need the scattering lengths of the different channels in the $F = 2$ manifold. According to [31], they are $a_0 = 87.4 \pm 1.0\,\mathrm{a_B}$, $a_2 = 92.4 \pm 1.0\,\mathrm{a_B}$ and $a_4 = 100.5 \pm 1.0\,\mathrm{a_B}$, with the Bohr radius $\mathrm{a_B} = 5.29 \cdot 10^{-11}\,\mathrm{m}$. In addition, we use the results of the direct measurements of the scattering lengths differences $a_2 - a_0 = 3.51 \pm 0.31\,\mathrm{a_B}$ and $a_4 - a_2 = 6.95 \pm 0.35\,\mathrm{a_B}$ by Widera et al. [32]. Plugging these values into equations (2.29) and (2.30) and converting into the one-dimensional couplings with the help of equation (2.19), we end up with $c_0 = 2\pi \cdot 2.635\,\mathrm{Hz}\,\mu\mathrm{m}$ and $c_1 = 2\pi \cdot 0.0849\,\mathrm{Hz}\,\mu\mathrm{m}$.
The experimentally extracted value of the spin interaction strength is $nc_1 = 2\pi \cdot 17.7\,\mathrm{Hz}$. This determines the magnitude of the quench parameter q which has to be chosen in order to address the different regimes of the Bogoliubov dispersion relation of the transversal spin excitations discussed in section 2.4.

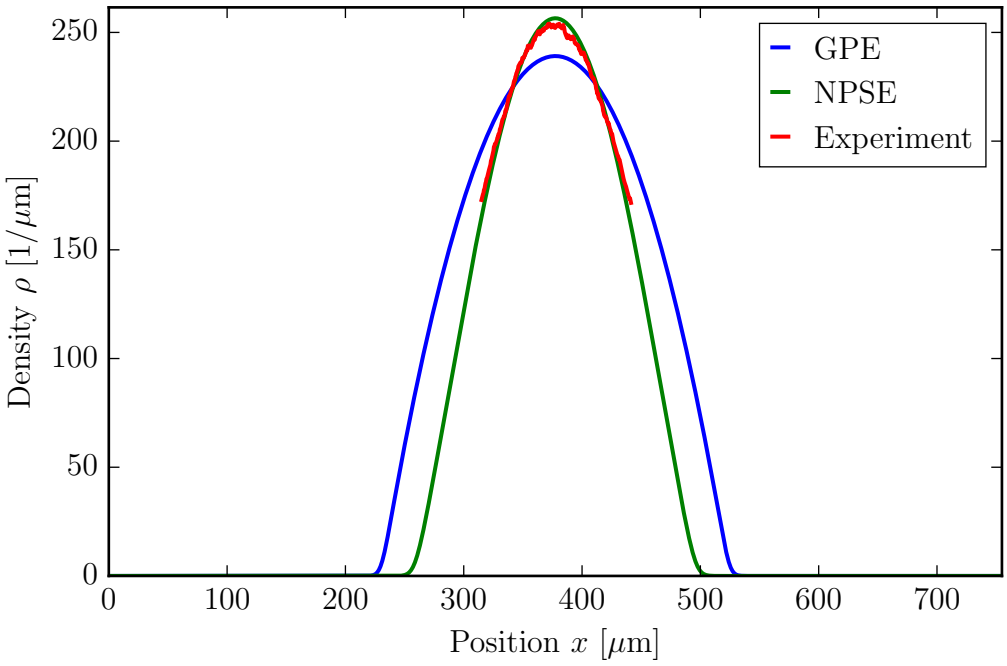

Figure 4.1: Comparison of the initial density profiles resulting from imaginary time propagation of the GPE (blue) and NPSE (green) with the experimental measured one (red). The trap is placed in the centre of the grid with a total grid size corresponding to $\sim 750\,\mu$m. The experimental data, averaged over several realisations, only covers a region of around $120\,\mu$m in the central part of the trap because of the limited imaging window. The NPSE result fits well to the experimental profile. The GPE cannot cover the experimental result since the shape of the profile is too broad. The narrowing of the NPSE profile is caused by transversal excitations. The total number of atoms in each simulation is adjusted such that 27000 atoms are in the inner $120\,\mu$m of the trap which coincides with the experimental mean atom number in this region.

4.2 GPE vs. NPSE

To enable a quantitative comparison between numerical simulations and experiments, we first investigate whether transversal excitations are present in the experimental setup. If excitations in the transversal direction of the trap play a role in the experiment, the dynamics should be well described by the quasi one-dimensional equations of motion given by the non-polynomial Schrödinger equations (2.23) - (2.25). If the experimental system is transversally in the ground state, the one-dimensional equations of motion which are the Gross-Pitaevskii equations (2.16) - (2.18) should give results which fit to the experimentally observed dynamics.

We start by comparing the initial density profiles emerging from imaginary time propagation of the GPE and NPSE with the experimental measured one. We expect different results for simulations of the GPE and NPSE as the state of minimal energy of the system depends on the conditions in transversal direction.
The density profiles for the different cases are depicted in Fig. 4.1. The total number of atoms in each simulation is adjusted such that 27000 atoms are in the inner 120 μm of the trap which coincides with the experimental mean atom number in this region. The trap is placed in the centre of the grid with a total grid size corresponding to $\sim 750\,\mu$m. The non-zero part of the density profiles spreads over 40% of the grid. The experimental data, averaged over several realisations, only covers a region of around 120 μm in the central part of the trap because of the limited imaging window. The profile resulting from imaginary time propagation of the NPSE fits well to the experimental profile. The GPE cannot cover the experimental results since the shape of the profile is too broad. The narrowing of the NPSE profile is caused by transversal excitations.
We can further study the presence of transversal excitations in the experimental setup by looking at dynamics on short timescales. The sudden parameter quench creates unstable momentum modes in the $m_F = \pm 1$ components, which lead to an exponential growth of the occupation numbers. A suitable observable to make comparison between simulation and experiment is the corresponding growth rate. The prediction for the evolution of the occupation numbers in the $m_F = \pm 1$ components made by homogeneous Bogoliubov theory is [6]

$$n_{k,\pm 1}(t) = \sinh^2\left[\gamma_{k,\pm 1} t\right], \tag{4.1}$$

where $\gamma_{k,\pm 1} = \mathrm{Im}\left(\omega_{k,\pm 1}\right)$ defines the growth rate of the momentum mode k as introduced in section 2.4.
We determine the growth rates of several unstable momentum modes by fitting a linear function to the corresponding logarithms of the occupation number spectra of the $m_F = 1$ component for $20\,\mathrm{ms} \leq t \leq 60\,\mathrm{ms}$. Due to the squared hyperbolic sine in equation (4.1), the growth rate is defined by

$$\gamma_{k,1} = \frac{\gamma_{k,1}^{\mathrm{fit}}}{2}, \tag{4.2}$$

where $\gamma_{k,1}^{\mathrm{fit}}$ is the slope of the linear fit.
A comparison of the growth rates extracted from simulations and the experimental data for three different quench parameters q is shown in Fig. 4.2. We study a regime where $k_{\mathrm{mu}} = 0$, since $-q < nc_1 = 17.7\,\mathrm{Hz}$. The blue solid line shows the growth rate predicted

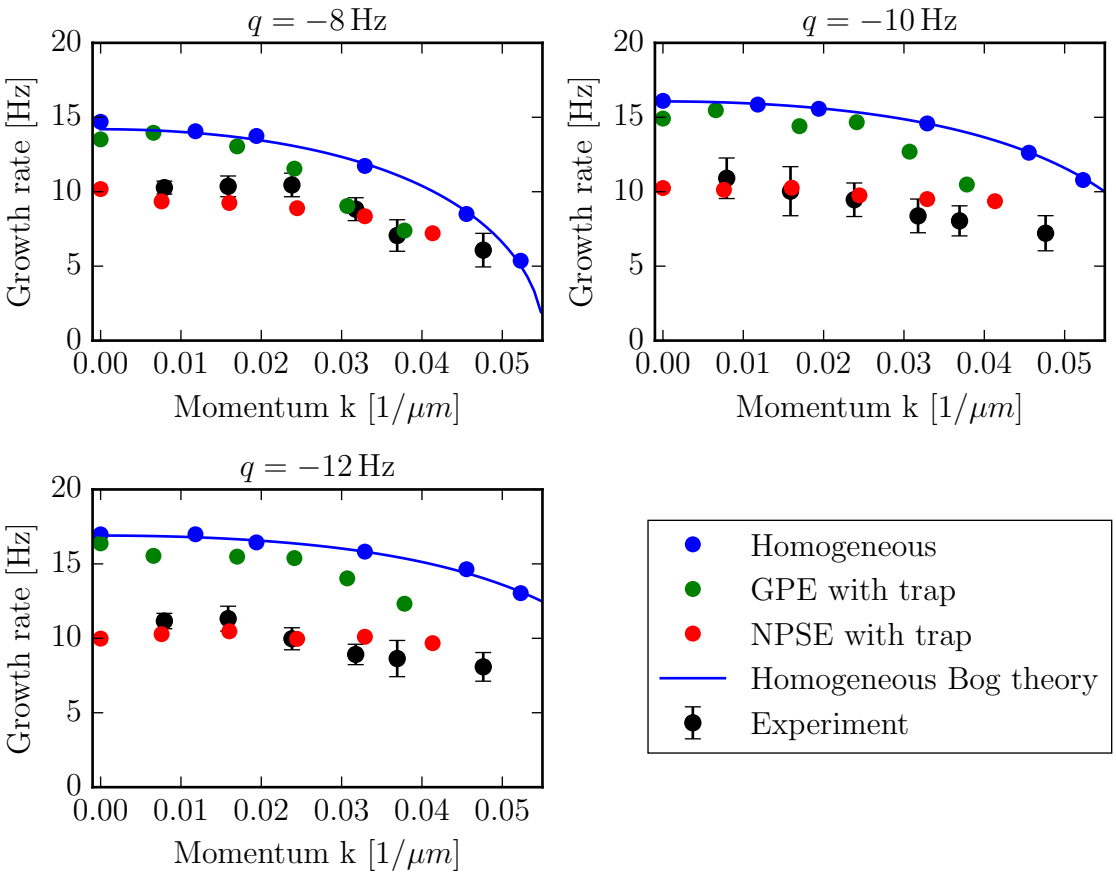

Figure 4.2: Comparison of the growth rates extracted from simulations and experimental data for three different quench parameters q. We are in a regime where $k_{\mathrm{mu}} = 0$, since $-q < nc_1 = 17.7\,\mathrm{Hz}$. The blue solid line displays the prediction made by homogeneous Bogoliubov theory. The blue dots are results from simulations in a homogeneous setup. They are solely used as a consistency check. The experimental results (black dots) deviate from the homogeneous predictions giving rise to modifications induced by the trapping potential. The growth rates resulting from GPE simulations (green dots) are close to the homogeneous setup for modes around $k_{\mathrm{mu}} = 0$. Thus the GPE cannot capture the experimental dynamics appropriately. The results obtained by NPSE simulations (red dots) fit to the experimental ones within error bars over the whole momentum region and for all three different q values. Thus the NPSE is more suited to recover the experimental dynamics. The error of the growth rates extracted from the simulations is as large as the dot size.

by homogeneous Bogoliubov theory and is given by

$$\gamma_{k,1} = \mathrm{Im}\left(\omega_{k,1}\right) = \mathrm{Im}\left(\sqrt{\left(\epsilon_k + q\right)\left(\epsilon_k + q + nc_1\right)}\right). \tag{4.3}$$

To make a consistency check, we first extract the growth rate for a homogeneous setting, i.e. we switch off the trapping potential in the simulation. The results (blue dots) fit well to the prediction in all three cases. The experimental growth rate (black dots) deviates from the homogeneous case, giving rise to modifications induced by the trapping potential. For $q = -10\,\mathrm{Hz}$ and $q = -12\,\mathrm{Hz}$ the growth rate remains nearly constant within error bars over the displayed momentum region. Turning to the results from GPE simulations (green dots), we find that, for modes close to the most unstable one, the growth rate reflects the one obtained in the homogeneous setup. For higher momenta it drops off and approaches the experimental data.
Due to the fact that the dynamics on short timescales is dominated by modes with the largest growth rates, the dynamics is not appropriately captured by the GPE. In contrast, the growth rates resulting from NPSE simulations (red dots) fit to the experimental ones within the error bars over the whole momentum region and for all three different q values. Thus, the quasi one-dimensional description by means of the NPSE is the more suited model to recover the experimental dynamics. We find that transversal excitations play an important role for the dynamics observed in the experiment.
In the following, we solely compare experimental data with results obtained with NPSE simulations.

4.3 Observables

As derived in section 2.4, the Bogoliubov excitations occur in the transversal spin direction. Thus a suited observable for analysing the short time dynamics is the transversal spin $F_\perp$ given by

$$F_\perp = F_x + iF_y. \tag{4.4}$$

The spin in x- and y-direction is calculated from the bosonic fields by

$$F_x = \frac{1}{\sqrt{2}} \frac{\left(\psi_0^* \left(\psi_1 + \psi_{-1}\right) + \left(\psi_1^* + \psi_{-1}^*\right) \psi_0\right)}{|\psi_1|^2 + |\psi_0|^2 + |\psi_{-1}|^2}, \tag{4.5}$$

$$F_y = \frac{i}{\sqrt{2}} \frac{\left(\psi_0^* \left(\psi_1 - \psi_{-1}\right) - \left(\psi_1^* - \psi_{-1}^*\right) \psi_0\right)}{|\psi_1|^2 + |\psi_0|^2 + |\psi_{-1}|^2}. \tag{4.6}$$

We expect the system to globally have no mean transversal spin. As the experimental data is extracted by imaging only the inner region of the entire trap, a non-zero mean value of the transversal spin can occur. Thus we subtract the mean value when comparing to experimental results.

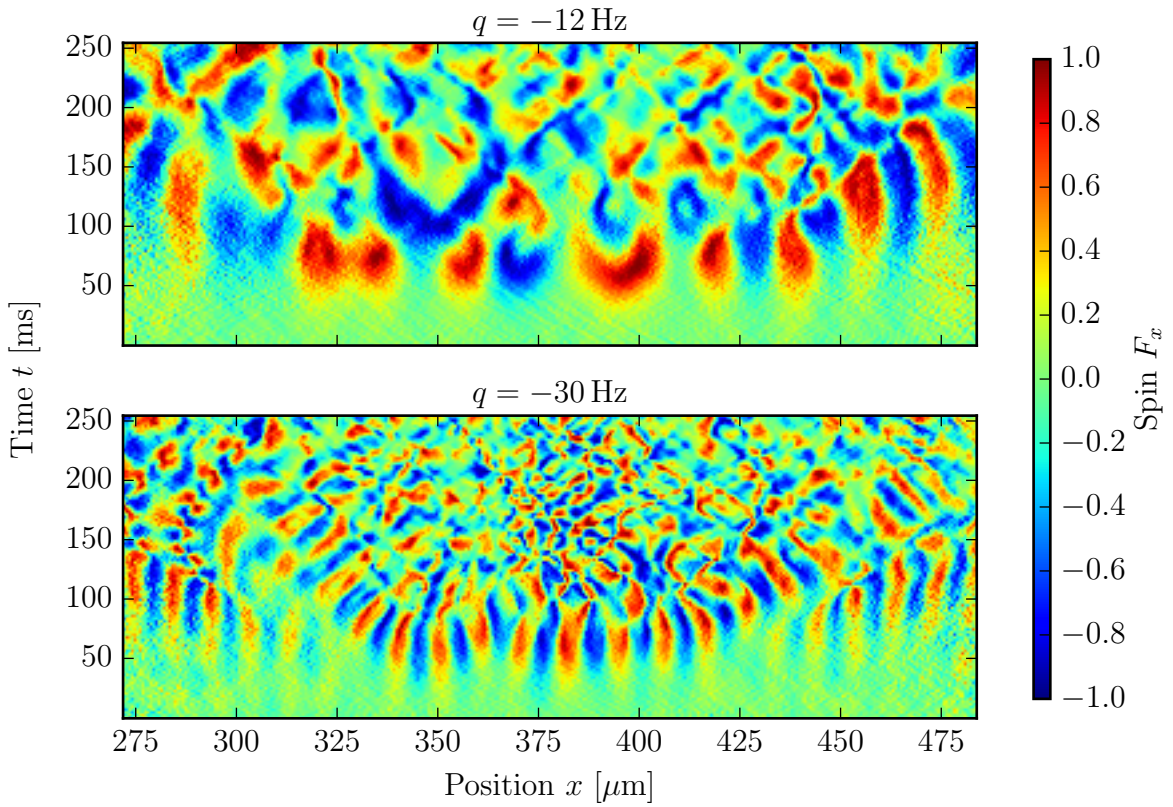

Figure 4.3: Time evolution of the F_x spin for a single run of the simulation. The resulting real space data is depicted for two different quench parameters q. The figure shows the central 210 μm of the trap. After 50 ms we see the formation of spin domains indicated by the red and blue areas. The initial domain size depends on the quench parameter. As the density is highest in the centre of the trap, the dynamics is faster in this region than in the outer ones. The structure size, extracted from the auto-correlation function of the transversal spin, can be associated with the spin domain size. During the time evolution, we find indications for a refining of the domain size.

Information about the instability region can be extracted from the transversal spin spectrum

$$G_{F_\perp,F_\perp}(k) = \langle F_\perp^*(k) F_\perp(k) \rangle = \left\langle |F_\perp(k)|^2 \right\rangle . \tag{4.7}$$

The most unstable momentum mode in transversal spin direction corresponds to the maximum of the spectrum.

Due to the direct relation between Fourier spectra and spatial correlation functions via the Wiener-Khinchin theorem [33], the same information can be extracted from the

auto-correlation function of the transversal spin given by

$$G_{F_\perp,F_\perp}(\Delta x) = \left\langle \sum_x F_\perp^*(x) F_\perp(x+\Delta x) \right\rangle . \tag{4.8}$$

We normalise the auto-correlation function to one at $\Delta x = 0$, such that $G_{F_\perp,F_\perp}(\Delta x) = 1$ indicates maximal correlation and $G_{F_\perp,F_\perp}(\Delta x) = -1$ maximal anti-correlation of the data.

Instead of the most unstable momentum mode, we determine the corresponding length scale $\xi = 2\pi/k_{\mathrm{mu}}$, which we define as twice the minimum of the auto-correlation function, i.e.

$$\xi = 2 \cdot \mathrm{argmin}\left[G_{F_\perp,F_\perp}(\Delta x)\right] . \tag{4.9}$$

Especially in the regime $0 < -q < nc_1$, where a broad range of unstable momentum modes grow with nearly the same rate, we can determine the structure size with a higher accuracy then the most unstable momentum mode.

To gain an impression of the physical meaning of the structure size, we analyse the real space data of the spin in x-direction for a single run of the simulation. Fig. 4.3 shows the time evolution of the F_x spin up to 250 ms for two different quench parameters $q = -12\,\mathrm{Hz}$ and $q = -30\,\mathrm{Hz}$. The figure displays a window of 210 μm in the centre of the trap. After 50 ms we see the formation of spin domains indicated by the red and blue areas. The initial domain size depends on the quench parameter. As the density is highest in the centre of the trap, the dynamics is faster in this region than in the outer ones. During the time evolution, we find indications for a refining of the domain size whose interpretation remains to be found. The minimum of the auto-correlation function can be associated with the depicted spin domain size because of anti-correlations emerging at spin domain walls.

4.4 Data analysis

To make direct quantitative comparison to the experimental results, we first match the numerical resolution on the grid to the experimental imaging resolution. Thus, we restrict the data analysis to a region of 120 μm around the centre of the trap. As the experimental resolution of $\sim 1\,\mu$m corresponds to 100 pixels in the analysis region, we bin as much of the grid points as necessary to end up with 100 simulation data points. We calculate the auto-correlation function and the Fourier spectrum of the transversal spin by making use of these data points.

The experiment does not allow accessing the wave functions, i.e. only densities can be measured. In view of equations (4.5) and (4.6), it turns out that we cannot directly image the transversal spin in the experiment. However, it is possible to extract this quantity after performing a spin rotation by means of a radio frequency magnetic field coupling, which rotates the spin vector around a random axis in the x-y-plane of the spin-1 sphere.
Rotating by $\pi/2$ maps the transversal spin onto the z-axis, such that it can be extracted via density measurements.
We mimic the experimental spin rotation by transforming the three component real space grid with the rotation matrix

$$\mathcal{R} = \exp\left\{-i\frac{\pi}{2}\left[f_x\cos(\phi) + f_y\sin(\phi)\right]\right\}, \tag{4.10}$$

where $f_{x,y}$ are the spin-1 matrices. The randomly chosen phase $\phi \in [0, 2\pi]$ reflects the randomness of the experimental rotation. The components of the rotated grid read

$$\psi_m^{\text{rotated}} = \mathcal{R}_{ml}\psi_l. \tag{4.11}$$

Thus, the transversal spin, which is mapped onto the z-axis, is given by

$$F_\perp = |\psi_1^{\text{rotated}}|^2 - |\psi_{-1}^{\text{rotated}}|^2. \tag{4.12}$$

When measuring observables in the experiment, detection noise has to be taken into account. We find that it can be modelled by Gaussian white noise. We can see the noise level in the Fourier spectra of the transversal spin which we discuss in the following section.

4.5 Emergence of structure at short times after a quench

In this section we investigate the emergence of structure at short times after a sudden parameter quench. Bogoliubov theory predicts unstable momentum modes in the transversal spin direction which can be analysed with the help of the Fourier spectrum of the transversal spin. Due to these instabilities, we observe spin domain formation in the transversal spin direction. The associated characteristic structure size of the system can be extracted from the auto-correlation function of the transversal spin.

To enable a quantitative comparison between numerical simulations and experiments, we mimic the experimental measurement of the transversal spin by performing a $\pi/2$ rotation of the grid around a random axis in the x-y-plane of the spin-1 sphere. We then bin our data points such that they fit to the experimental imaging window and resolution. Finally, we add Gaussian white noise to model the experimental detection noise.

We start with a direct comparison of simulation and experiment by analysing the auto-correlation functions and Fourier spectra of the transversal spin for short evolution times. The simulations are performed with the two different samplings of the initial quantum noise introduced in section 3.5.

Subsequently we compare numerical simulations with the homogeneous Bogoliubov theory derived in section 2.4. We expect that the structure of the system on short timescales is well described by the Bogoliubov prediction in the quench parameter regime $-q > nc_1$. For later evolution times deviations from Bogoliubov theory are anticipated as we are no longer in the regime of a small depletion of the condensate in the $m_F = 0$ component.

Comparing simulations with experiments

For the quantitative comparison of simulations with experiments, we exemplarily show results for the quench parameters $q = -12\,\mathrm{Hz}$ and $q = -22\,\mathrm{Hz}$. The predicted corresponding most unstable momentum modes are $k_{\mathrm{mu}} = 0$, and respectively $k_{\mathrm{mu}} = \sqrt{-2M\left(q + nc_1\right)/\hbar^2}$. We select four evolution times, namely $60, 80, 100$ and $120\,\mathrm{ms}$.

Fig. 4.4 and 4.6 display the auto-correlation functions of the transversal spin. The three different graphs correspond to the experimental data (EXP, red) and numerical NPSE simulations with initial quantum noise set into Fourier modes (NFM, green) as well as into the single particle eigenmodes of the effective potential for the $m_F = \pm 1$ components (NEP, blue). For a detailed description of the noise sampling see section 3.5. The error bar corresponds to the standard deviation of the mean values. The numerical results are averaged over 1000 runs.

Analysing the minima of the auto-correlation function in Fig. 4.4, we find that the corresponding structure size for simulations performed with the Fourier mode noise sampling at $t = 60\,\mathrm{ms}$ fits to the experimentally observed value at $t = 120\,\mathrm{ms}$. Thus the structure formation is way faster than in the experiment when sampling the noise into Fourier modes. As expected, we cannot simply use the noise sampling of the homogeneous setup.

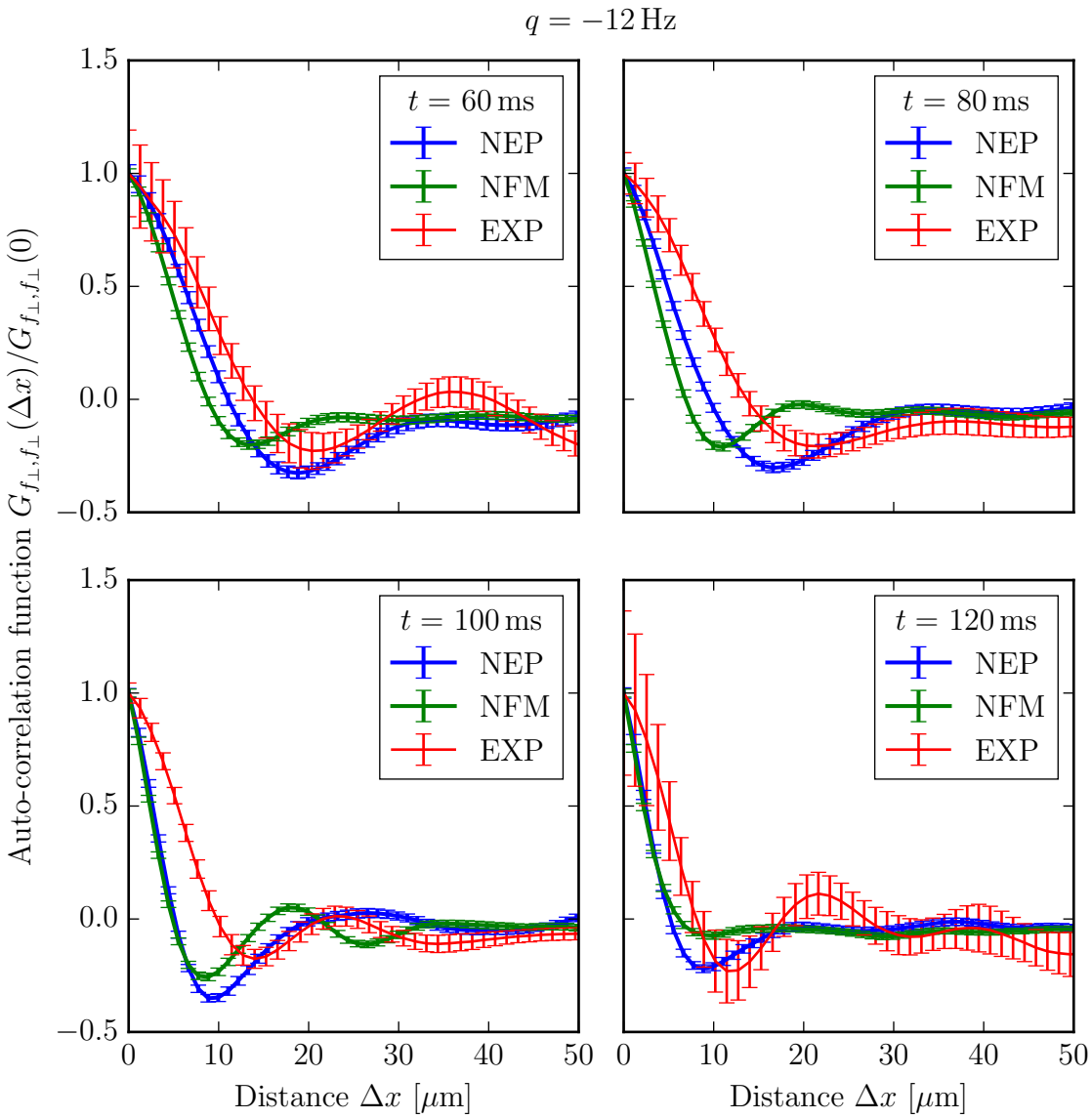

Figure 4.4: Auto-correlation function $G_{f_\perp,f_\perp}(\Delta x)$ (equation (4.8)) of the transversal spin normalised to $G_{f_\perp,f_\perp}(0)$ for the quench parameter $q = -12\,\mathrm{Hz}$ and four different evolution times t. The simulations performed with the initial noise set into Fourier modes (NFM, green) show a structure formation which is way faster than in the experiment. For $t = 60\,\mathrm{ms}$ the results of simulations with the initial noise set into the single particle eigenmodes of the effective potential (NEP, blue) are in good agreement with the experiment (EXP, red). For later times we see deviations arising, especially in the structure size of the system corresponding to the minimum of the auto-correlation function. In general, the slopes at short distances show different behaviours when comparing experiment and simulations. The error bar corresponds to the standard deviation of the mean values. The numerical results are averaged over 1000 runs.

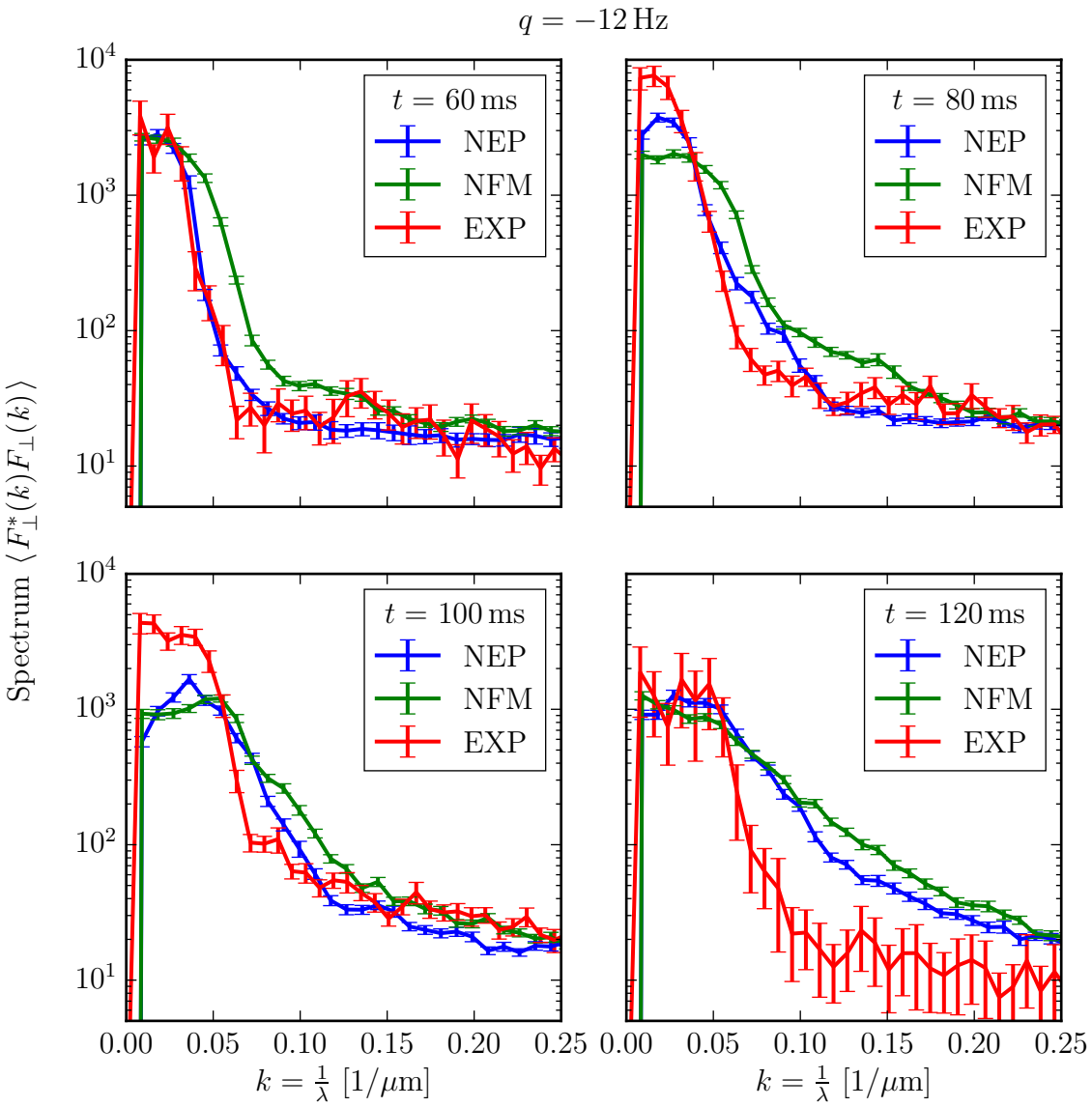

Figure 4.5: Fourier spectrum $\langle F_\perp^*(k) F_\perp(k) \rangle$ (equation (4.7)) of the transversal spin for the quench parameter $q = -12\,\mathrm{Hz}$ and four different evolution times t. For $t = 60\,\mathrm{ms}$ the results of simulations with the initial noise set into the single particle eigenmodes of the effective potential (NEP, blue) fit to the experiment (EXP, red) within error bars. For later times we see, that the lowest momentum modes grow faster in the experiment than in the simulation, which lead to larger experimentally observed structure sizes (see Fig. 4.4). In addition, the region of highly occupied momentum modes is broader in the simulations, which causes the damping of the oscillations in the autocorrelation function at large distances. The error bar corresponds to the standard deviation of the mean values. The numerical results are averaged over 1000 runs. The displayed momenta are divided by 2π.

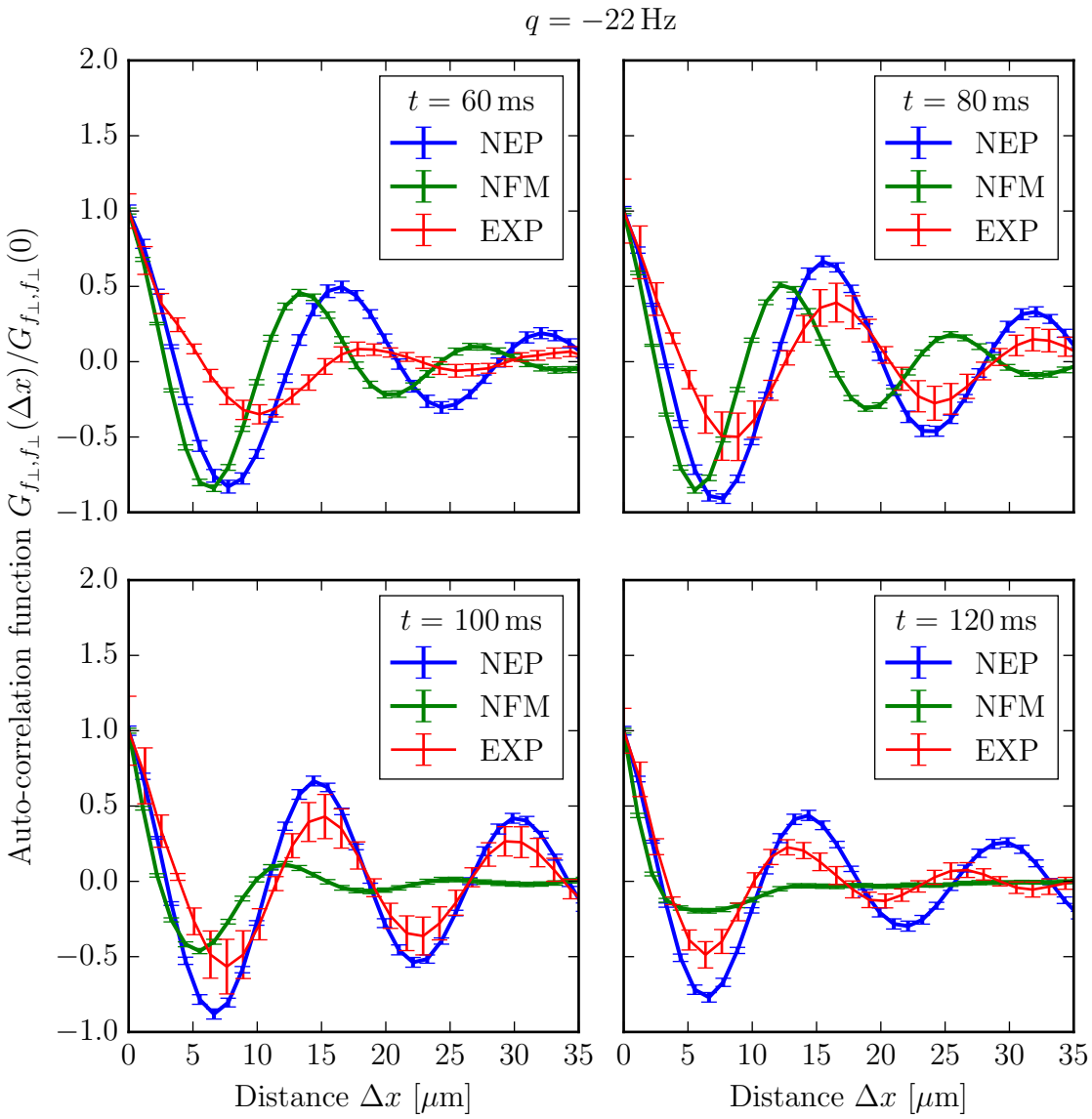

Figure 4.6: Auto-correlation function $G_{f_\perp,f_\perp}(\Delta x)$ (equation (4.8)) of the transversal spin normalised to $G_{f_\perp,f_\perp}(0)$ for the quench parameter $q = -22\,\mathrm{Hz}$ and four different evolution times t. The simulations performed with the initial noise set into Fourier modes (NFM, green) show a structure formation which is way faster than in the experiment. For $t = 80\,\mathrm{ms}$ and $t = 100\,\mathrm{ms}$ the results of simulations with the initial noise set into the single particle eigenmodes of the effective potential (NEP, blue) are in good agreement with the experiment (EXP, red). For $t = 60\,\mathrm{ms}$ we see deviations in the structure size of the system corresponding to the minimum of the auto-correlation function. In general, the slopes at short distances show different behaviours when comparing experiment and simulations. The error bar corresponds to the standard deviation of the mean values. The numerical results are averaged over 1000 runs.

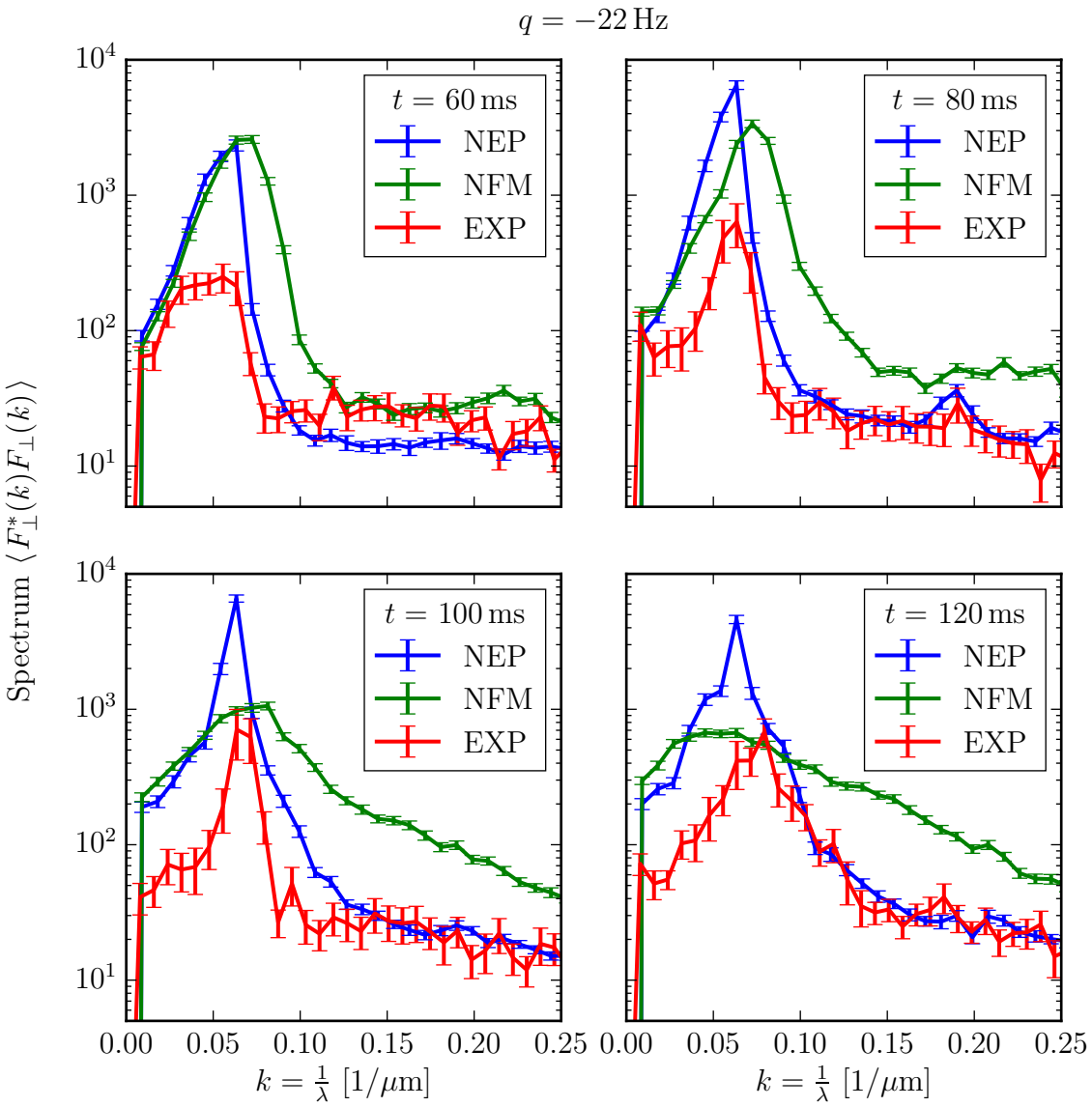

Figure 4.7: Fourier spectrum $\langle F_\perp^*(k) F_\perp(k) \rangle$ (equation (4.7)) of the transversal spin for the quench parameter $q = -22\,\mathrm{Hz}$ and four different evolution times t. For $t = 80\,\mathrm{ms}$ and $t = 100\,\mathrm{ms}$ the results of simulations with the initial noise set into the single particle eigenmodes of the effective potential (NEP, blue) are in good agreement with the experiment (EXP, red). For $t = 60\,\mathrm{ms}$ we see, that the region of highly occupied momentum modes is broader in the experiment than in the simulation, which leads to larger experimentally observed structure sizes and a damping of the oscillations in the auto-correlation function at large distances (see Fig. 4.6). The error bar corresponds to the standard deviation of the mean values. The numerical results are averaged over 1000 runs. The displayed momenta are divided by 2π.

Using the single particle eigenmodes of the effective potential for the $m_F = \pm 1$ components as an initial noise configuration, the numerical results (NEP, green) are in good agreement with the experimental ones (EXP, red) at specific times. For $q = -12\,\mathrm{Hz}$, the minimum of the auto-correlation function coincides with the experimental one within error bars at $t = 60\,\mathrm{ms}$, whereas we see deviations at later times. In contrast, for $q = -22\,\mathrm{Hz}$, the numerical results fit to the experiment at $t = 80\,\mathrm{ms}$ and $t = 100\,\mathrm{ms}$, whereas deviations are present at $t = 60\,\mathrm{ms}$.
In general, there are clearly visible differences in the initial slope of the auto-correlation functions. Additionally we find that the curve shapes of the auto-correlation functions at large distances Δx are different between simulations and experiment as oscillations are varyingly strong damped.
Analysing the corresponding spectra, depicted in Fig. 4.5 and 4.7, we can identify the origin of these deviations. In contrast to the experiment, the lowest momentum modes do not grow that fast in the simulation, although they are populated with noise. This leads to smaller structure sizes than in the experiment. Furthermore, the damping of the oscillations at large distances Δx is related to the width of the region of highly occupied momentum modes. The broader the region the larger is the damping of the oscillations. This effect can exemplarily be seen in the auto-correlation function and the spectrum for both quench parameters at $t = 120\,\mathrm{ms}$.
It is important to note that in the presented spectra the momenta are divided by 2π to allow for a direct comparison between the most unstable momentum mode and the structure size as they are solely related by taking the inverse.

Comparing simulations with Bogoliubov theory

In the following we compare NPSE simulations with the initial noise set into the single particle eigenmodes of the effective potential for the $m_F = \pm 1$ components to the homogeneous Bogoliubov theory (see section 2.4).
After 80 ms the population of the $m_F = \pm 1$ components contain more than 30 % of the total atom number. Thus the Bogoliubov approximation should only be valid for the results obtained after 60 ms and respectively break down for later times. We can get a first impression of possible deviations from Bogoliubov theory at later times by looking at the time evolution of the auto-correlation function respectively the Fourier spectrum plotted into a single graph as shown in Fig. 4.8. We find that the structure size gets smaller in time, which corresponds to shifting the highly occupied unstable momentum modes outwards to larger values.

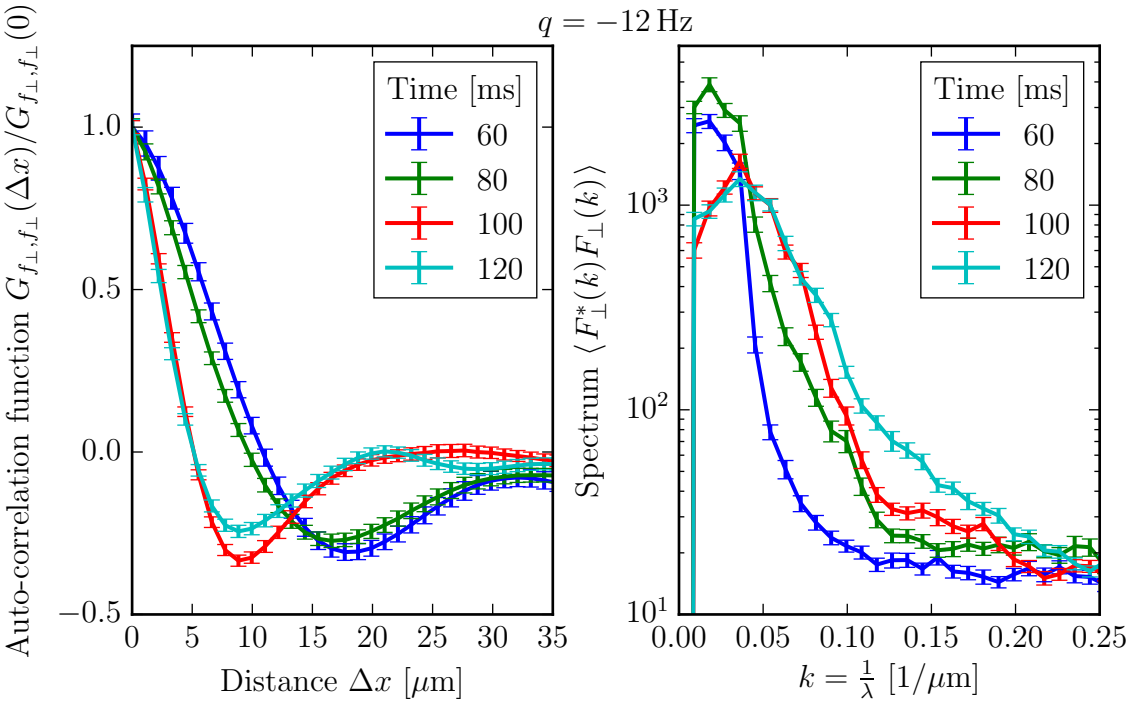

Figure 4.8: Time evolution of the normalised auto-correlation function and the Fourier spectrum of the transversal spin for the quench parameter $q = -12\,\mathrm{Hz}$. The results are obtained from numerical simulations with the initial noise set into the single particle eigenmodes of the effective potential for the $m_F = \pm 1$ components. We find that the structure size, which is related to the minimum of the auto-correlation function, gets smaller in time, which corresponds to shifting the highly occupied unstable momentum modes outwards to larger values. The error bar illustrates the standard deviation of the mean values. The numerical results are averaged over 1000 runs. The displayed momenta are divided by 2π.

We test our hypothesis by extracting the structure size from the auto-correlation function of the transversal spin over a wide range of quench parameters between $q = -2\,\mathrm{Hz}$ and $q = -30\,\mathrm{Hz}$. This is done by determining the minimum after cubic interpolation of the data.

Fig. 4.9 displays the results obtained for all four selected evolution times. The extracted structure size is depicted with blue dots, where the dot size is as large as the error. The green solid line (Bog fit) shows a fit of the homogeneous Bogoliubov theory to the data points for $-30\,\mathrm{Hz} \leq q \leq -20\,\mathrm{Hz}$ with

$$\xi = \frac{2\pi}{k_{\mathrm{mu}}} = \frac{2\pi}{\sqrt{-2M\left(q + nc_1\right)/\hbar^2}}, \tag{4.13}$$

where the spin interaction strength nc_1 is our fitting parameter. The black dashed line marks the fitted value of nc_1. The red solid line (Bog initial) is deduced from equation (4.13) by inserting the initial mean value of $nc_1 = 13.5 \pm 0.2\,\mathrm{Hz}$, which can be calculated from the NPSE density profile of the entire trap region depicted in Fig. 4.1.
For $t = 60\,\mathrm{ms}$, we get a fit value of $nc_1 = 13.7 \pm 0.3\,\mathrm{Hz}$, which coincides with the initial mean value within error bars. Hence, the data follows the homogeneous Bogoliubov prediction in the given regime of the quench parameter.
Although the initial NPSE density profile and the growth rates for small quench parameters are in good agreement with the experimental data (see Fig. 4.1 and 4.2), we find a different spin interaction strength than the experimentally extracted $nc_1 = 17.7\,\mathrm{Hz}$ for the shortest selected evolution time (see [14]).
This coincides with differences of the growth rates at short times in experiment and simulation arising in the quench parameter regime $-q > nc_1$. We find a strong damping of the growth rates in the experiment when going to quench parameters below $-30\,\mathrm{Hz}$, whereas the growth rates only decrease slightly in the simulations. We have seen first indications of this behaviour in the auto-correlation function for $q = -22\,\mathrm{Hz}$ at $t = 60\,\mathrm{ms}$ (see Fig. 4.4). A possible explanation is given by a quantum mechanical overlap argument between the condensate and the excitations. The smaller the wavelength of the excitations the less the overlap with the condensate, which would correspond to a damping of the growth rates for large negative values of the quench parameter.
Turning to later evolution times, we expect deviations from the Bogoliubov prediction. However, fitting the structure size for the same quench parameter regime with equation (4.13) shows that the data is again well described by the homogeneous Bogoliubov theory with a smaller value of nc_1. For $t = 80\,\mathrm{ms}$, we get $nc_1 = 12.2 \pm 0.3\,\mathrm{Hz}$, for $t = 100\,\mathrm{ms}$, we find $nc_1 = 10.3 \pm 0.3\,\mathrm{Hz}$ and for $t = 120\,\mathrm{ms}$, we have $nc_1 = 8.6 \pm 0.4\,\mathrm{Hz}$.
As the relevant fitting regime only corresponds to a small area of the displayed structure size, it is hard to check the quality of the fit by solely looking at Fig. 4.9. Additionally, plotting the associated squared most unstable momentum as a function of the quench parameter q gives access to the quality of the fit as the relevant regime is enlarged. In Fig. 4.10, the squared most unstable momentum is depicted with blue dots. The green solid line (Bog fit) shows the fit of the homogeneous Bogoliubov theory to the data points for $-30\,\mathrm{Hz} \leq q \leq -20\,\mathrm{Hz}$. We find that the data is well described by Bogoliubov theory at $t = 60\,\mathrm{ms}$ and $t = 80\,\mathrm{ms}$. Deviations at later times indicate a crossover from the Bogoliubov regime to dynamics beyond Bogoliubov.

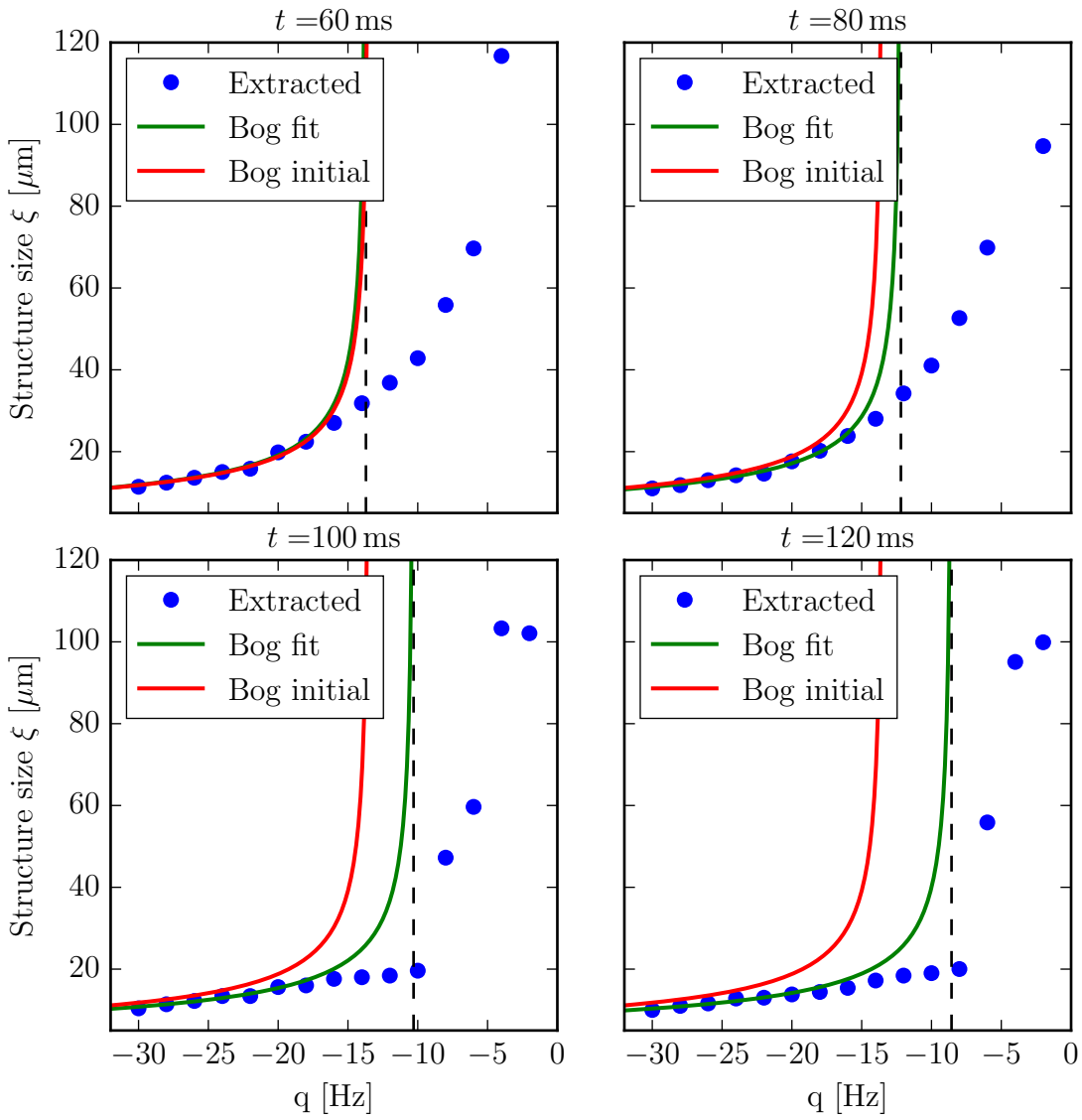

Figure 4.9: Comparison of the structure size (blue dots), extracted from the autocorrelation function of the transversal spin, with the Bogoliubov prediction. The green solid line (Bog fit) shows a fit of the homogeneous Bogoliubov theory to the data points for $-30\,\mathrm{Hz} \leq q \leq -20\,\mathrm{Hz}$. The black dashed line marks the fitted value of nc_1. The red solid line (Bog initial) is deduced from the initial mean value of $nc_1 = 13.5 \pm 0.2\,\mathrm{Hz}$. For $t = 60\,\mathrm{ms}$, we get a fit value of $nc_1 = 13.7 \pm 0.3\,\mathrm{Hz}$, which coincides with the initial mean value within the error. At later times, we find that the data is again well described by Bogoliubov theory with a smaller value of nc_1. For $t = 80\,\mathrm{ms}$, we get $nc_1 = 12.2 \pm 0.3\,\mathrm{Hz}$, for $t = 100\,\mathrm{ms}$, we find $nc_1 = 10.3 \pm 0.3\,\mathrm{Hz}$ and for $t = 120\,\mathrm{ms}$, we have $nc_1 = 8.6 \pm 0.4\,\mathrm{Hz}$. We attribute the observed shift to a smaller spin interaction strength nc_1 to the depletion of the $m = 0$ component due to spin-changing collisions. The structure size is limited by the window size of $\sim 120\,\mu\mathrm{m}$ because of the smallest momentum mode in the trap being larger than zero. The error of the extracted structure size is as large as the dot size.

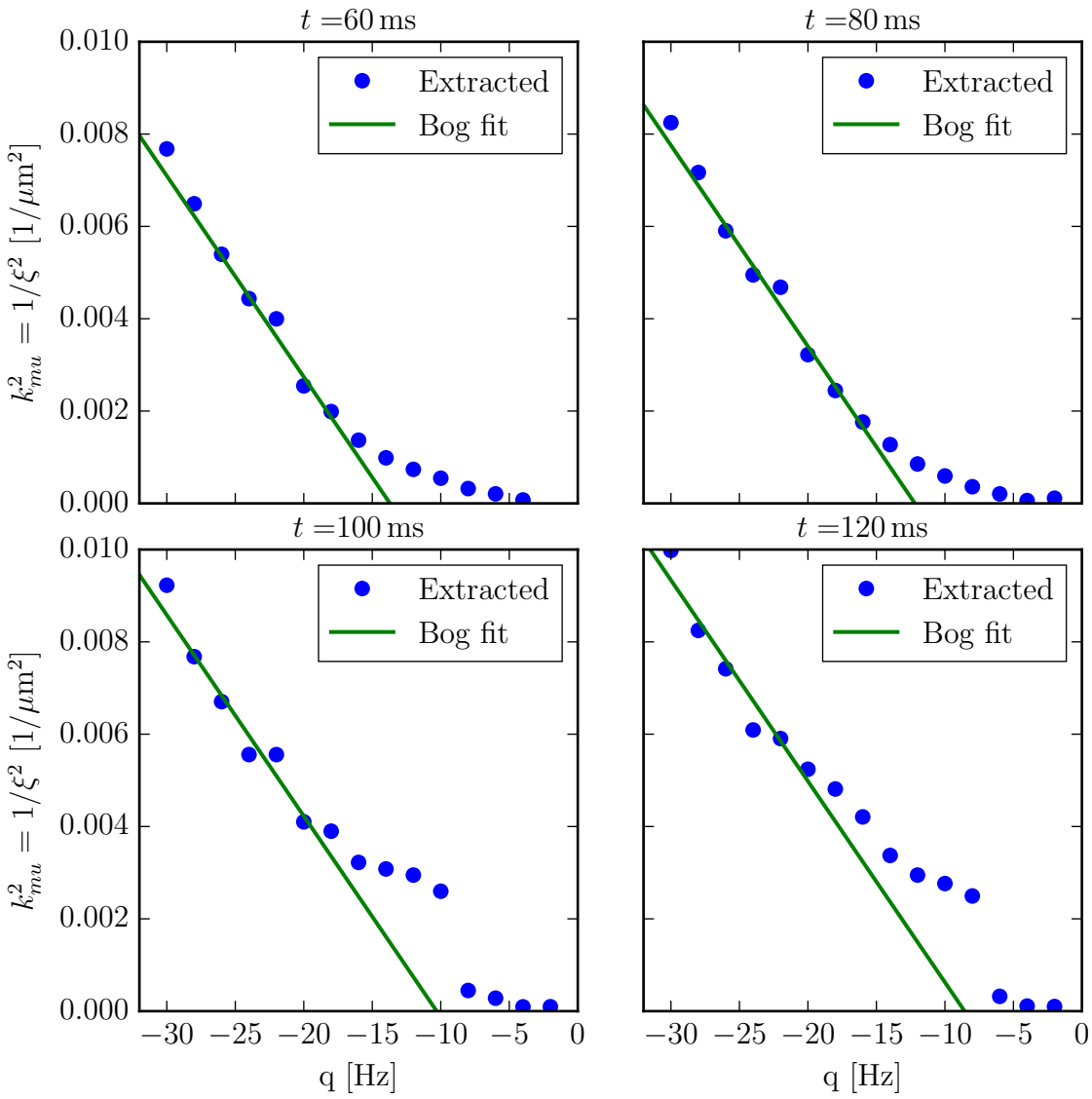

Figure 4.10: Comparison of the squared most unstable momentum (blue dots), associated with the extracted structure size, with the Bogoliubov prediction. The green solid line (Bog fit) shows a fit of the homogeneous Bogoliubov theory to the data points for $-30\,\mathrm{Hz} \leq q \leq -20\,\mathrm{Hz}$. Plotting the data in this form gives the possibility to check the quality of the fit as the relevant regime is enlarged compared to the data depicted in Fig. 4.9. We find that the data is well described by Bogoliubov theory at $t = 60\,\mathrm{ms}$ and $t = 80\,\mathrm{ms}$. Deviations at later times indicate a crossover from the Bogoliubov regime to dynamics beyond Bogoliubov. The error of the squared most unstable momenta is as large as the dot size.

In the discussed Bogoliubov approximation (see section 2.4), the density n is solely given by the density in the $m_F = 0$ component. As this component is depleted due to

spin-changing collisions, the spin interaction strength nc_1 is shifted to smaller values in time. Thus we find that the structure size of the system at later times can be described by the homogeneous Bogoliubov theory with a smaller spin interaction strength.
So far, we have analysed the structure sizes in the quench parameter regime $-q > nc_1$. For $0 < -q < nc_1$, the most unstable momentum mode in the homogeneous case is given by $k_{\mathrm{mu}} = 0$, which would correspond to a structure size which is as large as the entire system. Due to the trapping potential, the smallest momentum mode is set by the extent of the condensate R_c, i.e.

$$k_{\mathrm{min}} = \frac{1}{2R_c} \approx \frac{1}{240\mu m} > 0, \tag{4.14}$$

where we extracted R_c from the NPSE density profile depicted in Fig. 4.1. Hence, we expect the structure size to grow with decreasing $|q|$ and to finally saturate at the window size of $\sim 120\,\mu$m. The displayed data in Fig. 4.9 demonstrate this behaviour for all selected evolution times.
To be able to make predictions in this quench parameter regime, it is necessary to solve the Bogoliubov de-Gennes equations for the spin-1 BEC confined in a trapping potential which will be part of future work.

In this chapter, we showed that the quasi one-dimensional description by means of the non-polynomial Schrödinger equation is the appropriate model to recover the experimental dynamics because transversal excitations are present in the experimental setup. As the Bogoliubov excitations occur in the transversal spin direction, the transversal spin is a suited observable to analyse the emergence of structure at short times after a sudden parameter quench. The characteristic structure size of the system can be extracted by means of the auto-correlation function of the transversal spin. We mimic the experimental measurement of the transversal spin by performing a $\pi/2$ rotation of the grid around a random axis in the x-y-plane of the spin-1 sphere. We then bin our data points such that they fit to the experimental imaging window and resolution. Finally, we add Gaussian white noise to model the experimental detection noise. With this at hand we were able to make a quantitative comparison between numerical simulations and experiments. Therefore we analysed the auto-correlation function and the corresponding Fourier spectra of the transversal spin for short evolution times. We presented results of simulations performed with the two different noise samplings introduced in section 3.5. We found that sampling the noise into the single particle eigenmodes of the effective

potential for the $m_F = \pm 1$ components leads to good agreement of the structure size between simulation and experiment for some of the selected evolution times. Using the Fourier mode sampling the structure formation in the simulation is way faster than in the experiment. Finally, we compared NPSE simulations with the initial noise set into the single particle eigenmodes of the effective potential for the $m_F = \pm 1$ components to the homogeneous Bogoliubov theory. At $t = 60\,\mathrm{ms}$, the structure size of the system follows the Bogoliubov prediction given by the initial mean value of the spin interaction strength nc_1 in the quench parameter regime $-q > nc_1$. Although the initial NPSE density profile and the growth rates for small quench parameters are in good agreement with the experimental data, we find a different spin interaction strength than in the experiment at $t = 60\,\mathrm{ms}$. For later times we expect deviations from Bogoliubov theory. However, we find that the structure size is again well described by Bogoliubov theory with a smaller spin interaction strength nc_1. We attribute the observed shift to a smaller spin interaction strength nc_1 in time to the depletion of the $m_F = 0$ component due to spin-changing collisions. Slight deviations from the Bogoliubov prediction at times $t > 100\,\mathrm{ms}$ indicate a crossover from the Bogoliubov regime to dynamics beyond Bogoliubov.

5 Conclusion and Outlook

In this thesis, we have numerically studied the emergence of structure in a (quasi) one-dimensional trapped spin-1 Bose gas at short times after a sudden quench. We compared our results to experiments performed with ^{87}Rb atoms in the $F = 2$ hyperfine manifold. By investigating the initial density profiles after imaginary time propagation as well as the growth rates of unstable momentum modes on short timescales, we showed that excitations in the transversal direction of the trap play an important role in the experimental setup. Thus we used the quasi one-dimensional description of the system by means of the non-polynomial Schrödinger equations, where transversal excitations are included, to make direct quantitative comparisons between simulations and the experiment.
To study the structure formation at short times after the quench, we analysed the auto-correlation function and the corresponding Fourier spectrum of the transversal spin. We extracted the characteristic structure size of the system, associated with the spin domain size in the transversal spin direction, from the minimum of the auto-correlation function. If we sample the initial quantum noise into Fourier modes, the structure formation in the simulation is way faster than in the experiment. We find that sampling the initial quantum noise into the single particle eigenmodes of the effective potential for the $m_F = \pm 1$ components leads to good agreement of the structure size between simulation and experiment for some of the selected evolution times. Nevertheless, we cannot exactly recover the experimental results for all evolution times.
To further improve the agreement between simulation and experiment we can study several experimental effects that are not included in our simulation so far.
When performing experiments with ultracold atoms which are confined in a trapping potential, particle loss has to be taken into account. The loss of particles leads to a decrease of the density which directly affects the dynamics of the system. As 66 % of the total atoms are left in the experiment after an evolution time of 500 ms, we expect the effects of particle loss on the dynamics at short timescales to be small.
In the experiment, the initial state in the polar phase is prepared at a finite temperature $T \sim 10\,\mathrm{nK}$. Thus thermal fluctuations are present in the initial configuration in addition

to quantum noise. Determining the ground state of the polar phase by means of imaginary time propagation does not include temperature effects. Including these effects into the simulation could lead to an adequate description of the initial experimental state. Consequently we would expect that the structure formation on short time scales agree with the experiment.

We found that the characteristic structure size of the system, extracted from numerical simulations, follows the homogeneous Bogoliubov prediction given by the initial mean spin interaction strength of the system for an evolution time of 60 ms in the quench parameter regime $-q > nc_1$. At later times, we observed that the data is well described by Bogoliubov theory with a shifted spin interaction strength nc_1. We attribute this to an effective change of the spin interaction strength due to the depletion of the $m_F = 0$ component.

Studying the properties of the system at evolution times beyond the Bogoliubov regime will be of future interest. For systems far from equilibrium, prethermalized states [34] as well as non-thermal fixed points [35, 36, 37] are predicted. In the vicinity of such non-thermal fixed points, universal properties of the system become visible [37, 38, 39, 40]. This is related to scaling behaviour of the physical observables [5].

Evaluating the scaling behaviour in space and time, we aim at identifying universal dynamics in the experimental setup. With our studies we hope to be able to benchmark experiment with simulations and vice versa which furthermore allows for examining their use as quantum simulators.

As we also have experimental access to ^{87}Rb in the hyperfine manifold $F = 1$, where we are dealing with ferromagnetic interactions as the spin-spin coupling c_1 is negative, we will investigate the properties of this system at evolution times beyond the Bogoliubov regime. For the two-dimensional case, scaling behaviour of the spatial correlation functions due to coarsening dynamics is predicted [41].

Comparing results obtained for the $F = 1$ system to the $F = 2$ system will give the possibility to directly extract the differences emerging by virtue of a sign change in the spin-spin coupling.

Of special theoretical interest will be the stability analysis of the Bogoliubov de-Gennes equations for a spin-1 BEC in the presence of a trapping potential. With this we will gain further insight into deviations from the homogeneous Bogoliubov theory arising in trapped systems. Furthermore, it would be interesting to compare results for one-dimensional settings with quasi one-dimensional ones as well as to observe the crossover region in between.

Bibliography

[1] L. E. Sadler, J. M. Higbie, S. R. Leslie, M. Vengalattore and D. M. Stamper-Kurn. "Spontaneous symmetry breaking in a quenched ferromagnetic spinor Bose–Einstein condensate". In: *Nature* 443 (2006).

[2] D. M. Stamper-Kurn and M. Ueda. "Spinor Bose gases: Symmetries, magnetism, and quantum dynamics". In: *Rev. Mod. Phys.* 85, 1191 (2013).

[3] Q. Gu and R. A. Klemm. "Ferromagnetic phase transition and Bose-Einstein condensation in spinor Bose gases". In: *Physical Review A* 68, 031604(R) (2003).

[4] H. Saito, Y. Kawaguchi, and M. Ueda. "Topological defect formation in a quenched ferromagnetic Bose-Einstein condensates". In: *Physical Review A* 75, 013621 (2007).

[5] E. Nicklas, M. Karl, M. Höfer, A. Johnson, W. Muessel, H. Strobel, J. Tomkovič, T. Gasenzer and M. K. Oberthaler. "Observation of Scaling in the Dynamics of a Strongly Quenched Quantum Gas". In: *Phys. Rev. Lett.* 115, 245301 (2015).

[6] Y. Kawaguchi, M. Ueda. "Spinor Bose-Einstein condensates". In: *Physics Reports* 520 (2012).

[7] C. Mora and Y. Castin. "Extension of Bogoliubov theory to quasicondensates". In: *Physical Review A* 67 (2003).

[8] E. Gross. "Classical theory of boson wave fields". In: *Annals of Physics* 4, no. 1 (1958).

[9] J. Berges, T. Gasenzer. "Quantum versus classical statistical dynamics of an ultracold Bose gas". In: *Physical Review A* 76 (2007).

[10] P. B. Blakie, A. S. Bradley, M. J. Davis, R. J. Ballagh and C. W. Gardiner. "Dynamics and statistical mechanics of ultra-cold Bose gases using c-field techniques". In: *arXiv:0809.1487v2 [cond-mat.stat-mech]* (2008).

[11] A. Polkovnikov. "Phase space representation of quantum dynamics". In: *arXiv: 0905.3384v3 [cond-math.stat-mech]* (2010).

[12] M. J. Steel, M. K. Olsen, L. I. Plimak, P. D. Drummond, M. Tan, M. J. Collett, D. F. Walls and R. Graham. "Dynamical quantum noise in trapped Bose-Einstein condensates". In: *Physical Review A* 58, Number 6 (1998).

[13] A. Sinatra, C. Lobo, Y. Castin. "The truncated Wigner method for Bose condensed gases: limits of validity and applications". In: *arXiv:cond-mat/0201217.v3 [cond-mat.stat-mech]* (2009).

[14] M. Prüfer. *Structure Formation in a Quenched Antiferromagnetic Spinor Bose-Einstein Condensate (Master thesis)*. (2016).

[15] Wenxian Zhang and L. You. "An effective quasi-one-dimensional description of a spin-1 atomic condensate". In: *arXiv:cond-mat/0412300v2 [cond-mat.other]* (2005).

[16] L. Salasnich, A. Parola and L. Reatto. "Effective wave equations for the dynamics of cigar-shaped and disk-shaped Bose condensates". In: *Physical Review A* 65, 043614 (2002).

[17] J. Vanier and C. Audoin. *The Quantum Physics of Atomic Frequency Standards*. Philadelphia: A. Hilger, (1988).

[18] S. Uchino, M. Kobayashi, M. Ueda. "Bogoliubov theory and Lee-Huang-Yang corrections in spin-1 and spin-2 Bose-Einstein condensates in the presence of the quadratic Zeeman effect". In: *Physical Review A* 61, 063632 (2010).

[19] M. A. Hillery, R. F. O'Connell, M. O. Scully, and E. P. Wigner. "Distribution functions in Physics: Fundamentals". In: *Physics Reports* 106 (1984), pp. 121–167.

[20] S. Sarra. "The Method of Characteristics with applications to Conservation Laws". In: *Journal of Online Mathematics and its Applications* (2003).

[21] J. A. C. Weidemann and B. M. Herbst. "Split-step methods for the solution of the nonlinear Schrödinger equation". In: *SIAM J. Numer. Anal.* 23, No. 3 (1986).

[22] G. Strang. "On the construction and comparison of difference schemes". In: *SIAM J. Numer. Anal.* 5, No. 3 (1968).

[23] J. M. Sanz-Serna and J. G. Verwer. "Conservative and Nonconservative Schemes for the Solution of the Nonlinear Schrödinger equation". In: *IMA Journal of Numerical Analysis* 6 (1986), pp. 25–42.

[24] E. J. Putzer. "Avoiding the Jordan canonical form in the discussion of linear systems with constant coefficients". In: *The American Mathematical Monthly* vol. 73 (1966).

[25] S. Heupts. *Non-equilibrium dynamics of an ultracold spin-1 Bose gas (Master thesis)*. (2014).

[26] A. Klenner. *A Study of Quench Dynamics in Ultracold Spinor Bose Gases in Comparison with Experiments (Master thesis)*. (2016).

[27] P. Bader, S. Blanes, F. Casas. "Solving the Schrödinger eigenvalue problem by the imaginary time propagation technique using splitting methods with complex coefficients ". In: *arXiv:1304.6845v2 [math.NA]* (2013).

[28] M. Scherer, B. Lücke, J. Peise, O. Topic, G. Gebreyesus, F. Deuretzbacher, W. Ertmer, L. Santos, C. Klempt and J. J. Arlt. "Spontaneous symmetry breaking in spinor Bose-Einstein condensates". In: *Physical Review A* 88, 053624 (2013).

[29] H. Saito, Y. Kawaguchi, and M. Ueda. "Topological defect formation in a quenched ferromagnetic Bose-Einstein condensates". In: *Physical Review A* 75, 013621 (2007).

[30] L. A. Williamson and P. B. Blakie. "Coarsening and thermalization properties of a quenched ferromagnetic spin-1 condensate". In: *Physical Review A* 94, 023608 (2016).

[31] D. M. Stamper Kurn, M. Ueda. "Spinor Bose gases: Symmetries, magnetism and quantum dynamics". In: *Rev. Mod. Phys.* 85 (2013).

[32] A. Widera, F. Gerbier, S. Fölling, T. Gericke, O. Mandel, I. Bloch. "Precision measurement of spin-dependent interaction strengths for spin-1 and spin-2 87 Rb atoms". In: *New Journal of Physics* 8 (2006).

[33] N. Wiener. "Generalized Harmonic Analysis". In: *Acta Mathematica* 55 (1930), p. 117.

[34] J. Berges, Sz. Borsányi, C. Wetterich. "Prethermalization". In: *Physical Review Letters* 93, 14 (2004).

[35] B. Nowak, S. Erne, M. Karl, J. Schole, D. Sexty, and T. Gasenzer. "Non-thermal fixed points: universality, topology and turbulence in Bose gases". In: *arXiv:1302.1448v1 [cond-math.quant-gas]* (2013).

[36] B. Nowak, D. Sexty, and T. Gasenzer. "Superfluid turbulence: Nonthermal fixed points in an ultracold Bose gas". In: *Physical Review B* 84 (2011).

[37] M. Karl, B. Nowak, and T. Gasenzer. "Universal scaling at non-thermal fixed points of a two-component Bose gas". In: *Physical Review A* 88 (2013).

[38] M. Karl, B. Nowak, and T. Gasenzer. “Tuning universality far from equilibrium”. In: *Scientific Reports* 3 (2013).

[39] M. Schmidt, S. Erne, B. Nowak, D. Sexty, and T. Gasenzer. “Non-thermal fixed points and solitons in a one-dimensional Bose gas”. In: *New Journal of Physics* 14, no. 7 (2012).

[40] B. Nowak, S. Erne, M. Karl, J. Schole, D. Sexty, and T. Gasenzer. “Non-thermal fixed points: universality, topology and turbulence in Bose gases”. In: *arXiv preprint arXiv:1302.1448* (2013).

[41] L. A. Williamson and P. B. Blakie. “Universal Coarsening Dynamics of a Quenched Ferromagnetic Spin-1 Condensate”. In: *Physical Review Letters* 116, 025301 (2016).

Danksagung

An dieser Stelle möchte ich mich bei all denjenigen bedanken, die mich bei der Anfertigung meiner Masterarbeit unterstützt haben.
Zuallererst danke ich Thomas Gasenzer, der mir die Möglichkeit gegeben hat an diesem spannenden Forschungsprojekt zu arbeiten und auch in Zukunft weiterhin arbeiten zu dürfen. Außerdem bedanke ich mich für die vielen interessanten Diskussionen und Gespräche.
Markus Oberthaler danke ich für die Übernahme der Zweitkorrektur und die zahlreichen Anregungen zum benchmarking von Theorie und Experiment.
Ein großer Dank geht an meinen Kollegen Markus, der sich immer wieder die Zeit genommen hat meine nicht endenden Fragen zur Numerik und theoretischen Konzepten zu beantworten. Außerdem möchte ich ihm für die vielen hilfreichen Korrekturen zu meiner Arbeit danken.
Ein spezieller Dank gilt meinem Kollegen Max vom BEC für die großartige Zusammenarbeit im letzten Jahr und die zahlreichen Aktivitäten fernab des Institutes. Ohne seine vielen Ideen und Anregungen wäre das gemeinsame Projekt weit weniger zielstrebig verlaufen. Ich freue mich auf die Zusammenarbeit in den kommenden Jahren.
Ich danke meinen Bürokollegen Stefanie, Markus, Martin und Halil für die angenehme Arbeitsatmosphäre und die zahlreichen Diskussionen zu allen erdenklichen Themen des Lebens.
Danke auch an den Teil der Arbeitsgruppe am ITP, die trotz der räumlichen Trennung immer für Fragen bereit standen.
Ebenso möchte ich mich bei allen Kollegen vom Experiment für die Einblicke in die experimentelle Arbeit sowie die zahlreichen gemeinsamen sportlichen Aktivitäten bedanken.

Zum Schluss geht ein ganz besonderer Dank an meine Familie, die mich immer in allen Lebenslagen unterstützt hat.

Erklärung

Ich versichere, dass ich diese Arbeit selbstständig verfasst und keine anderen als die angegebenen Quellen und Hilfsmittel benutzt habe.

Heidelberg, den 28. Oktober 2016